DÉPARTEMENT
DE GÉOSCIENCES

Master internship report

Supervised by Sigrún Hreinsdóttir[2] and Ian Hamling[2]

Crustal deformation using GPS and InSAR analysis at Taupo volcano, New Zealand

Cyril Journeau[1]

July 31, 2018

1: Département de Géosciences, Ecole Normale Supérieure, PSL Res. Univ., Paris, France
2: GNS Science, Lower Hutt, New Zealand

Abstract

Taupo Volcano, located in the central part of the TVZ (Taupo volcanic Zone), North Island of New Zealand, is one of the most productive Rhyolitic centres in the world. Although its last eruption occurred about 1800 years ago, 16 periods of unrest have been identified including surface deformation, hydrothermal eruptions, and seismic swarms since 1870. The town of Taupo lies on the north-eastern shore of the lake filling the caldera of the volcano and is located close to recent seismic swarms and local surface deformation episodes highlighted in this report.
The aim of this internship is to study the different periods of episodic deformation, contrasting with the long-term deformation of the Taupo region, in order to constrain the sources generating local deformation. For this, an analysis of GPS (continuous and campaign stations) and InSAR data (from two satellites, EnviSAT and ALOS) was conducted. After correcting the data for several external factors such as subsidence generated by water pumping in the Wairakei-Tauhara geothermal station and displacements associated with slow slip events along the Hikurangi subduction interface, periods of local deformation have been identified. We highlight two periods of uplift with rates of 10 mm/yr in 2004-2008 and in 2011-2013 accompanied by more or less rapid horizontal deformation punctuated by seismic swarms.
The geodetic data were inverted to characterize the deformation sources using the GBIS software, allowing the use of different analytical models. In order to explain the different periods of deformation over time, at least three sources at different locations are needed, revealing the presence of different processes at depths ranging from $\sim$ 10 km to $\sim$ 0.5 km and whose causes can vary given the complexity of the tectonic context characterizing the region.

Résumé

Le volcan Taupo, situé dans la partie centrale de la TVZ (Taupo volcanic Zone), île du Nord de Nouvelle Zélande, est l'un des plus productifs centres rhyolitiques au monde. Bien que sa dernière éruption ait eu lieu il y a environ 1800 ans, 16 périodes d'instabilités ont été identifiées incluant de la déformation en surface, des éruptions hydrothemales ainsi que des essaims sismiques depuis 1870. La ville de Taupo se trouve sur la rive nort-est du lac remplissant la caldera du volcan, à proximité de récents essaims sismiques et d'épisodes de déformation locale mis en évidence dans ce rapport.
Le but de ce stage est d'étudier les différentes périodes de déformation épisodiques, contrastant avec la déformation observée sur le long-terme de la région de Taupo afin de contraindre les sources générant de la déformation locale. Pour cela, une analyse des données GPS (stations continues et de campagne) et InSAR (issues de deux satellites, EnviSAT et ALOS) a été menée. Après avoir corrigé les données de plusieurs facteurs externes tels que la subsidence générée par l'extraction d'eau dans les stations géothermales Wairakei-Tauhara et les déplacements associés aux évènements de glissement lents le long de l'interface de subduction d'Hikurangi, certaines périodes de déformation locale ont été identifiées. Nous mettons en évidence deux périodes de soulèvement crustal avec des vitesses de 10 mm/yr en 2004-2008 et en 2011-2013 accompagnées de déformation horizontale plus ou moins rapide ponctuée par des essaims sismiques.
Les données géodésiques ont été inversées afin de caractériser les sources de déformation en utilisant le logiciel GBIS, permettant l'utilisation de divsers modèles analytiques. Afin d'expliquer les différentes périodes de déformation au cours du temps, au moins trois sources à des localisations différentes sont nécessaires, révélant la présence de différents processus à des profondeurs variant de $\sim$10 km à $\sim$0.5 km et dont les causes peuvent varier étant donné la complexité du contexte tectonique caractérisant la région.

Contents

1 Introduction **2**

1.1 Regional settings: Geodynamic and Geophysical context 2

1.2 Taupo volcano 2

2 Data and methods **4**

2.1 GPS data 4

2.1.1 GPS principle 4

2.1.2 GPS processing 6

2.1.3 GPS post-processing 7

2.2 InSAR data 7

2.2.1 InSAR principle 7

2.2.2 InSAR processing 9

2.2.3 InSAR post-processing 10

2.3 Data analysis 11

2.3.1 External influences 11

2.3.2 Local deformation 13

3 Modeling and interpretation **15**

3.1 Modeling strategy 15

3.2 Results 15

3.2.1 2004-2008 period 15

3.2.2 2005-2007 period 16

3.2.3 2007-2011 period 17

3.2.4 2011-2015 period 19

4 Discussion and conclusion **20**

References **23**

1 Introduction

1.1 Regional settings: Geodynamic and Geophysical context

The North Island of New Zealand lies astride a tectonic plate boundary where the Pacific plate subducts obliquely beneath the Australian plate at rates of 38-49 mm/yr (Beavan et al., 2002; DeMets et al., 2010). Its active tectonics are dominated by this subduction at the Hikurangi Trench, the back-arc rifting along the TVZ (Taupo Volcanic Zone) and the strike-slip faulting through the NIDFB (North Island Dextral Fault Belt), (Figure 1.1). TVZ, which covers an area of $\sim$ 6000 km^2, has been active since 2 Ma, and is considered as the largest and most frequently active rhyolitic magmatic system on Earth (Wilson et al., 1995). Rifting has localised along extensive NE-SW trending fault belts (Villamor and Berryman, 2001) with total extension rate estimated from GPS measurements varying from $\sim$15 mm/yr at the Bay of Plenty to $<$ 5 mm/yr south of Lake Taupo (Wallace et al., 2004). Based on different styles of volcanism, the TVZ is segmented into three parts: the northern and southern segments are dominated by andesite volcanism with the central 125-km-long segment, predominantly rhyolitic. It comprises eight caldera centres including Taupo and Okataina, the world's most active rhyolitic volcanoes (Rowland et al., 2010). Another major caracteristic of the TVZ is the high heat flux that reaches the surface through his numerous geothermal fields. This flux of 700-800 mW/m^2 is anomalously high for continental crust and in addition to the conductive heat transport, a component is thought to be related to repeated intrusions into the crust (Bibby et al., 1995). Based on seismic velocity models, the crust under the TVZ central part is estimated to be $\sim$ 16 km thick, with highly conductive regions below $\sim$ 8-10 km deep, interpreted as large bodies of partial melt (Stratford and Stern, 2006; Heise et al., 2010). Seismic activity across the TVZ is characterized by numerous shallow earthquakes located in the top 8 km of the crust, indicating a brittle-ductile transition at about that depth (Bryan et al., 1999).

1.2 Taupo volcano

Taupo volcano has been active for $\sim$ 300 ka, with a more frequent and intense activity over the last 65 ka. The present caldera was formed by the Oruanui Eruption 27,000 years ago, generating $\sim$ 430 km^3 of fall deposits and 300 km^3 of pyroclastic material. It was modified by the last eruption around 1800 years ago (Taupo Eruption) with vents located along a NE-SW-trending fissure centred on the Horomatangi Reef. To date, 28 small eruptions have been identified between these two majors eruptions (Sutton et al., 2000; Wilson, 2001). The caldera is now filled by Lake Taupo which makes deformation studies challenging. The results of a

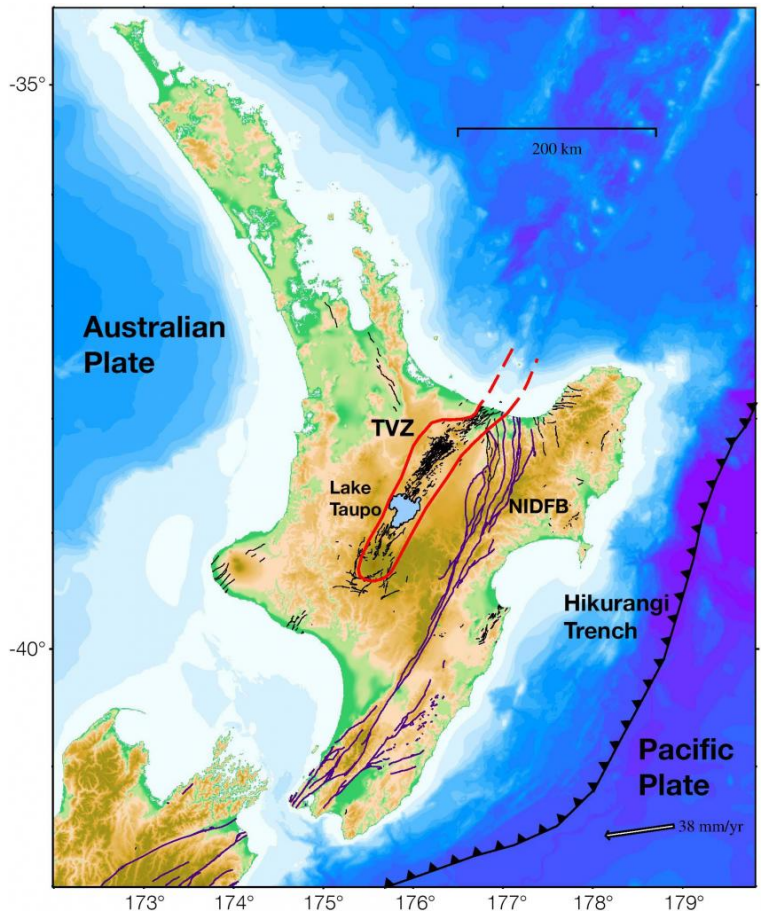

Figure 1.1: Colour shaded relief map of the North Island, New Zealand. We can see the location of the plate boundary between the Pacific and Australian plates marked by the Hikurangi Trench. The red line is the modern TVZ boundary -with activity during and since the 65 ka eruption of Okataina Volcanic Centre (Wilson et al., 1995)- in which the active extensive faults are represented by the black lines. Also the NIDFB fault is visible in indigo.

gravity survey show that the most intense negative Bouguer gravity anomaly in the TVZ is located over the northern part of the lake which is interpreted to outline the area of caldera collapse (Davy and Caldwell, 1998).

Ellis et al. (2007) summarizes the modern geophysical studies (shallow resistivity, heat-flow measurements, MT anomalies, seicmic velocities, receiver functions) conducted at Taupo volcano to determine its present state. These results don't indicate the presence of a large magma body (tens to hundreds of km^3) within the mid-crust (4-8 km). However, the results are ambiguous because of the lake's presence, limiting the measurement coverage, and the low-velocity and weak volcanoclastic deposits near the surface degrade the signal quality for seismological studies. They point out that the crust may contain small pockets of partial melt that can not be detectable by the techniques mentioned above.

Heat flow measurements made in the sediments at the bottom of Lake Taupo reveal high heat flows (> 120 mW/m^2) in nine separate areas of the lake. The two largest are centred on the Horomatangi Reef, corresponding to the location of the largest low resistivity area and the

main vent area for the Taupo Eruption (Whiteford, 1996; Caldwell and Bibby, 1992). Moreover, De Ronde et al. (2002) found that active hydrothermal venting occurs beneath this geothermal system.

It is necessary to continuously monitor Taupo volcano in order to identify any instability periods that may be related to an activation of the magmatic or hydrothermal system and eventually lead to hazards. Potter et al. (2015) listed 16 unrest episodes between 1872 and 2010, including hydrothermal eruptions, seismic swarms and vertical deformation. The most recent one in this catalogue occured between 2008 and 2010. Figure 1.2 shows the distribution of shallow seismicity (< 20 km) between 2002 and 2018 (GeoNet catalogue). It is localized in some places and often appears in seismic swarm. We also see that seismicity increases significantly: between 2008 and 2010 (this corresponds to the period mentioned above) and in 2017 when hundreds of small earthquakes were recorded in the southwest of the lake without apparent deformation. Peltier et al. (2009) used numerical modelling in order to interpret leveling data acquired on the lake between 1979 and 2007. The results reveal a long-term subsidence punctuated by strong short-term uplift. The long-term subsidence is explained by both crust stretching and a deep deflation source while the uplift is interpretated by the movement of rhyolitic magma or pressurization of the shallow hydrothermal fluid reservoir depending on the depth of the source.

Since 2001, Taupo has been monitored by GeoNet providing earthquake data and maintaining and operating continuous GNSS stations around the lake. The TAUP station was installed in 2002 and shows that these short-period variations mentioned by (Peltier et al., 2009) are a continuing feature of the volcano (see Figure 2.2). Additional nine stations were installed from 2006.

In this study, we conduct an analysis of recent GPS and InSAR data. We use data from the ten GNSS stations combined with campaign data acquired in 2005, 2007, 2011 and 2015, as well as InSAR data from Envisat and ALOS satellites covering respectively the 2003-2011 and 2007-2011 time periods. The aim of the study is to understand what are the sources of the observed deformation. The main issues are to identify periods of local deformation in the data and to extract some information on the magma plumbing system for these periods. For that, we model the geodetic data using a Bayesian inversion to estimate deformation source parameters: location, depth, volumetric changes and geometry.

2 | Data and methods

2.1 GPS data

2.1.1 GPS principle

GNSS (Global Navigation Satellite System) operation is based on the precise measurement of the time propagation of a signal emitted by the satellites to a receiver, allowing us to determine

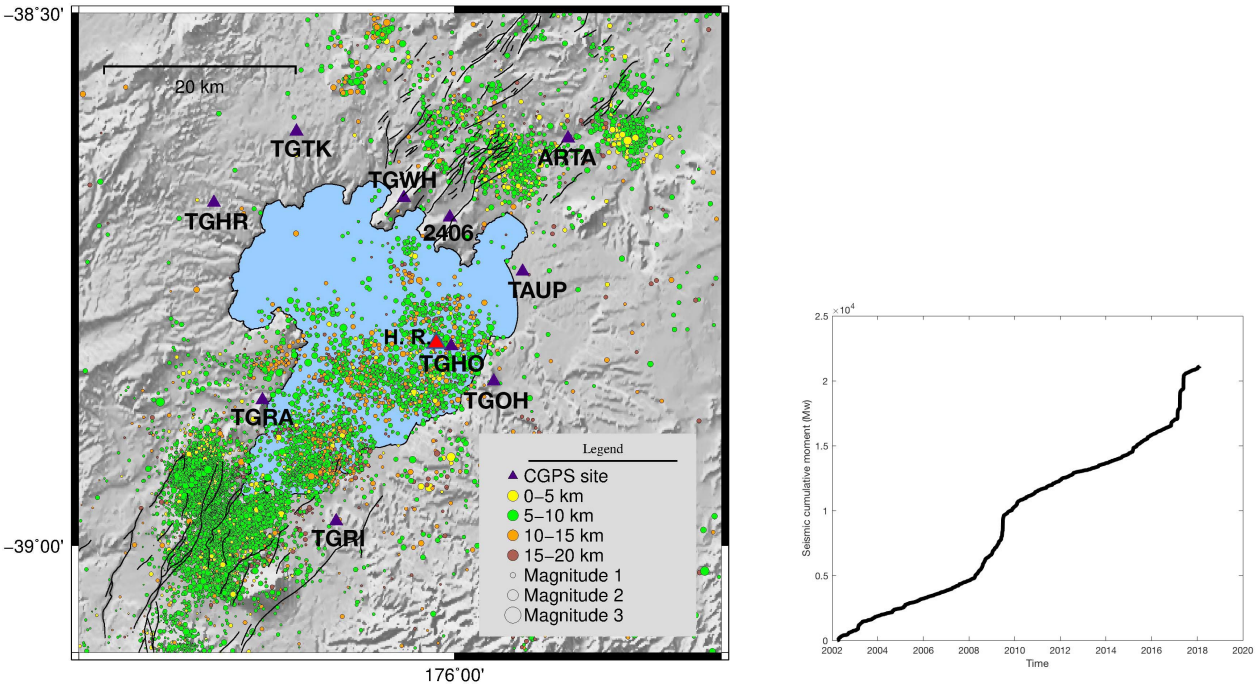

Figure 1.2: Left figure: Distribution of the shallow seismicity (< 20 km) from GeoNet catalogue and the CGPS network. The red triangle stand for the Horomatangi Reef. Right figure: Representation of the seismic cumulative moment over time for the same area represented in the left figure.

the distance that separates them. In this study, we used GPS (Gobal Positioning System) data which is the system owned by the United States government and opertared by the United States Air Force. The distance between the receiver and the satellite is given by the formula $D = \int c.dt$ where c is the speed of light in the propagation medium (variable in the ionosphere and the troposphere). The satellites emitt signals on two to three electromagnetic waves L1, L2 and L3 of frequency 1575.42, 1227.60 and 1381.05 MHz respectively, called carrier frequencies. They are modulated by codes including the code P (Precise code) and C/A (Coarse/Acquisition Code). The receiver receives a coded signal emitted by the satellites. It synthesizes in turn a code identical to that of the satellite and it can calculate the time between the arrival of the satellite signal and the synthesized signal. The receiver-satellite distances obtained from the signal modulated by the codes are called pseudo-distances. However, the accuracy of these pseudo-distances is not sufficient for earth science applications where millimeter accuracy is required. In order to gain the precision, the phase measurement technique is used: satellite-station distance measurements are made directly on the carrier wave of each GPS signal. This gives a very accurate but ambiguous measurement of the propagation time of the signal. Indeed, we only know the number of wave oscillations separating two measurements made on the same satellite at two different times and not the number of oscillations separating the satellite from the antenna. The signal phase therefore comprises two parts, the ambiguous one and the phase difference between two different times. Also, the measurement is accompanied by

several errors: signal interaction with atmosphere (we differenciate ionosphere and troposphere refraction), positioning accuracy of GPS satellites, the clocks accuracy (satellites and receivers) and the phase center position of GPS ground and satellite antennas. It is therefore necessary to process the raw data in order to take into account these errors and to remove the ambiguity. The application of the double difference technique (by using data from at least two receivers and two satellites) allows us to overcome clocks errors, giving us baselines lengths, i.e. the distances separating the different stations used. It will then be necessary to connect the measured network to a reference frame. Crossing the ionosphere, the propagation time of the GPS wave is disturbed because of the presence of charged particles (ionospheric delay) affecting the frequencies differences. In order to estimate at first order this delay, the two carriers L1 and L2 of different frequencies are used. Part of the delay is removed by making a linear combination of the phase difference measurements of the two carriers. However, the delay induced by the troposphere is not frequency dependent. Also others factors are taken into account such as ocean tidal effects, precession and nutations movements of the Earth around its axis of rotation.

2.1.2 GPS processing

The raw data from the receivers are transformed into RINEX (Receiver Independant Exchange Format Version) files using the TEQC software. Then we process the data using the GAMIT/-GLOBK version 10.6. First, GAMIT (Global Positioning System At Massachusetts Institute of Technology) is used in order to calculate baselines between all the stations from phases differences. This includes severals steps using differents modulus. The calculation of the baselines is done by least-squares inversion of the data (phase differences), the goal being to find the parameters of a model (which correspond to the adjustments made to our knowledge a priori) minimizing the residuals, i.e. the differences between the data and the model. For all the data used in this study, the calculation has been done in RELAX mode where the positions of both satellites and stations are not fixed. Thus, the solved parameters are the station coordinates, satellite orbit, Earth rotation parameters, estimating atmospheric zenith delays every 2 h and using three atmospheric gradients per day. The International GNSS Service 2014 azimuth and elevation-dependent absolute phase center model was used for all antennas, with an elevation cutoff angle of 10° for the ground-based antennas in order to limit the layer of atmosphere crossed and the effects of multipath. Also, the Finite Element Solution 2004 (FES04) ocean loading model was applied to correct for ocean loading.

Secondly, GLOBK is used to connect the stations and to evaluate their displacements in the ITRF 2014 reference frame. Its origin is located at the mass center of the system Earth/GPS satellites constellation. Over 100 stations from ITRF were analyzed with the data allowing us to constrain the solution as their position and velocity are known. Based on a Kalman filter, the GLOBK software adjusts station positions and velocities to those of the ITRF stations, taking

into account previously estimated baseline lengths. Finally, the time series were generated with the *glred* program of GLOBK, giving the position evolution of a site in time, for each component, with respect to the first position measurement.

2.1.3 GPS post-processing

In this study, 10 continuous stations located around the Taupo Lake are used to investigate local deformation at Taupo volcano. To better constrain the deformation field, we also use a dozen of sites measured during field campaigns conducted in the TVZ in 2005, 2007, 2011 and 2015 (see Figure 2.1). Once the time series have been generated, we detrend them in order to remove long-term tectonic signals. The long-term trend is estimated with *Tsview*, a GGMatlab tool allowing interactive viewing and manipulation of GPS time series (Herring, 2003). We have also estimated and removed annual and semi-annual period oscillations corresponding to seasonal deformation. However it seems that there are still annual variations in the vertical component (Figure 2.2), these seasonal terms are probably not optimally estimated because of the many "breaks" inserted in the time series associated with offsets in the data. It can also be complicated because of the presence of the lake and geothermal systems that can add variations. The study of the detrended time series allows us to emphasize offsets in the time series linked to episodic deformation events that can be of different nature: large distant earthquakes, slow slip events (SSE), rifting processes, fault movements, magmatic or hydrothermal processes. In Figure 2.1 we can see the estimated background velocity field which we use to correct the data for. This steady background deformation has been estimated from all the time series of the continuous sites by removing outliers and putting "breaks" in the time series where offsets are present in order to get a confident estimation of the "inter-event" behaviour. Then we extrapolate values for the campaigns sites using the closest neighbours. Before extrapolating, we estimated the velocity on the 2011-2015 period considerated as relatively stable (at least for stations enough far away from the 2012 event location presented in the section 2.3.2) for both continuous and campaigns sites to compare their behaviour and check if it is a relevant choice. We decided to not use the campaigns sites located near the Wairakei-Tauhara geothermal station (Figure 4.1) because of the subsidence induced by water pumping which affect them (as discussed later in the part 2.3.1). This background deformation can be interpreted as the long-term expression of the rift extension for this area.

2.2 InSAR data

2.2.1 InSAR principle

RADAR (RAdio Detection And Ranging) is an active remote sensing technique using electromagnetic waves in the microwave domain (wavelength of 0.056 and 0.236 meters for Envisat's and ALOS's radars respectively). An antenna emits a signal that is scattered by the target

and is then recorded when it is returned to the antenna. SAR (Synthethic Aperture Radar) is a form of radar processing whereby a large synthetic antenna is simulated by combining the radar returns from consecutive radar pulses. The principle is based on the analysis of the phase variation of the signal reflected by an object when there is a change in the measurement position, using a RADAR antenna on a satellite or an airplane. When the radar moves over an area, the same target on the ground is scanned several times with a varying angle and a relative position.

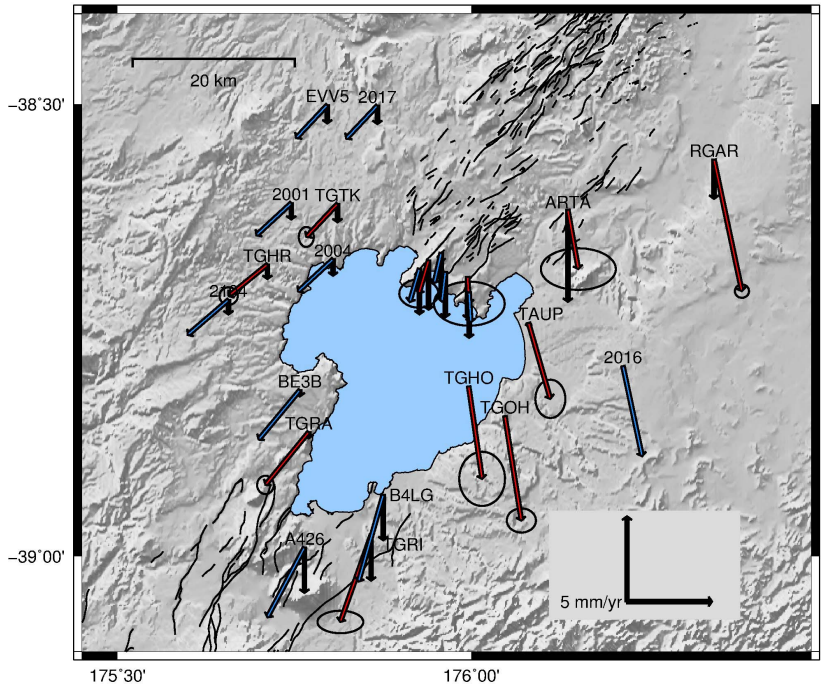

Figure 2.1: Background field velocity of the region estimated from continuous GPS sites (red colors) and interpolated for campaigns sites (blue colors). Velocities are expressed in the Australian fixed reference frame. Black arrows stand for the vertical component. For the sake of visibility, station names located north of the lake are indicated here from west to east: 1 = 2010, 2 = TGWH, 3 = 2009, 4 = 2407, 5 = 2406, 6 = 2012.

A SAR image has two components: the amplitude (A), which is the intensity of the back-scattered signal picked up by the antenna which depend on the backscattering coefficient of the target; and the phase (expressed as $\phi = \frac{4\pi}{\lambda} R[2\pi]$ where R is the sensor-target distance and λ the wavelength) containing distance information between the satellite and the illuminated pixel. It is not actually a geometric distance but a differential phase measurement between incident and reflected signals. InSAR (Interferometric Synthetic Aperture Radar) is a radar technique used in geodesy and telemetry that requires at least two SAR images acquired at a different time or at the same time from two orbits, separated by a distance called "baseline". The principle of this technique is to combine the phase of the two SAR images: by taking the difference of these phases, one can obtain the satellite-ground distance difference (ΔR) between the two passes of the satellite or between the two orbits used. This gives an image of the phase difference, called interferogram. However, the interferometric phase is the sum of several components and

the extraction of that including the ground deformation ($\Phi_{def} = \phi_1 - \phi_2 = \frac{4\pi}{\lambda}\Delta R[2\pi]$) requires several steps of processing. We note that $\Phi = \Phi_{def} + \Phi_{topo} + \Phi_{flat} + \Phi_{atm} + \Phi_{orbit} + \Phi_{noise}$. Φ_{topo} is due to the topography which introduces look angle variation resulting in a phase difference between two points not being at the same altitude. This component is simulated and eliminated using a DEM (Digital Elevation Model). Doing so, another residual phase is introduced almost entirely due to error in the DEM used which will be taken into account in the processing. Φ_{flat} is due to range distance variations across the image. This component is corrected using satellite orbits in the interferogram flattening step (correction is applied as if the scattering surface were lying on a reference ellipsoid). Φ_{atm} is the atmospheric component related to a delay in the radar signal as it propagates through the atmosphere. Φ_{orbit} is linked to errors in the orbital information. Its residual part is treated after the interferogram formation. Φ_{noise} is mainlty due to a loss of coherence.

2.2.2 InSAR processing

In this study, data were processed and analysed from two satellites: Envisat, with ascending tracks 151 and 380 and ALOS with ascending and descending tracks 326 and 628, respectively. (see Table 2.1 to an information summary about these tracks). Envisat data were analysed following the method of Hooper et al. (2007) with *StaMPS* while ALOS data were analysed following the method of Hooper (2008) with *StaMPS/MTI*, an extended version allowing a combined multi-temporal InSAR method. These two methods allow us to generate InSAR time series, they are briefly presented here but the processing details can be found in the two previous references. The first one is only based on the Persistent Scatterer (PS) approach, the goal being to achieve the selection of stable, intrinsically coherent pixels throughout the duration of the study. PS candidates are selected based on their backscatter properties: they are identified as a resolving cell whose response is dominated by a single bright target and stable on the ground. Thus, the variance in the phase, as well as in the backscattering intensity due to relative movement of different diffusers is reduced. The second method combined the PS one with the Small Baseline (SB) approach. The first step is to focuse raw data and create SLC (Single-Look Complex) image using ROI-PAC software. Then the DORIS software is used to form N interferograms from N+1 SLC images with respect to the same master image. This interferogram generation for the PS processing differs in some ways from the conventional interferogram formation. The master image is chosen so as to maximize the sum correlation of all the interferograms by minimizing the acquisition time interval, the perpendicular baseline and the difference in Doppler centroid, corresponding to the Doppler shift at antenna beam centre (see Figure 4.6 where the master image is the one for which the perpendicular baseline is 0). Slave images are coregistred using an amplitude based algorithm in order to keep a good correlation by estimating offsets in position between pairs of images. Then each image

is resampled to the master coordinate system and the phase difference between the master and each image is computed. Because of spatial differences of acquisition between master and slave images, geometric phase correction is applied leading to additional errors: look angle error (combination of DEM error and difference in range between the position of the dominant scatterer and the center of the pixel) and squint angle error, treated as noise. Finally every pixel position is estimated in a geocoded reference frame. Here, topographic corrections were made using the NASA Shuttle Radar Topography Mission DEM (SRTM DEM). Once the interferograms are formed, a first PS candidate pixels selection is achieved based on amplitude analysis and then based on phase analysis to estimate pixels phase stability through an iterative process. Then these informations are used to compute the probability than a pixel is a PS pixel. Once the selection is done, some spatially uncorrelated parts of the signal are substracted before unwrapping the phase using SNAPHU and then the master and slaves contributions to the spatially correlated phase are estimated. Finally, the signal due to deformation in the PS pixels can be isolated.

The SB method aims to generate interferograms in which the perpendicular, temporal and Doppler baselines between the SAR pairs used to generate interferograms are minimized in order to obtain more correlated interferograms. To do this, we construct a network connecting all the SAR image pairs without isolated clusters (see Figure 4.7). So in this case there are combinations with different master images which imply the need of precise resampling of the interferograms to the exactly same position. Before the formation of these interferograms, both filtering in range and in azimuth are applied to reduce geometric decorrelation and to discard non-overlapping Doppler frequencies respectively. As mentionned by Hooper (2008), the method aims to identify the slowly-decorrelating filtered phase (SDFP) pixels, those whose phase when filtered shows little decorrelation over short time intervals. Then, both PS and SB techniques are merged: the equivalent SB interferogram phase to the PS pixels is calculated by recombination of single-master interferogram phase and there is a combination of the SB interferogram phase from both PS and SDFP pixels. The resulting phase is corrected for spatially-uncorrelated look angle error and is unwrapped. The unwrapped phases are inverted in order to generate the InSAR time series for each pixel by directly using a Least-Square adjustment. Some interferograms showing local phase-unwrapping errors are dropped from the inversion.

2.2.3 InSAR post-processing

Some residual orbital errors affecting the results were estimated and removed by fitting a linear plane from each interferogram in the time series. Also, to account for the atmospheric error due to the variable water vapor distribution, an empirical correction based on the relation between topography and water vapor content was applied. Then, InSAR data were aligned to the GPS

reference frame by adjusting them to conform to non-detrended GPS estimates of LOS rate. Next we removed the tectonic background deformation estimated from GPS data in order to analyse coherent deformation signals. Comparisons of LOS displacement between the InSAR and GPS time series are shown in the Figures 4.3 and 4.5 respectively for the tracks 151 and 628. Finally, we estimated the LOS mean velocity by solving for the best-fitting displacement rate x such as $A^T\Sigma^{-1}Ax = A^T\Sigma^{-1}b$ where the A matrix contains the time interval of each epoch relative to the master epoch, the b matrix containts the displacements at each epoch for each scatterer and Σ is the temporal variance-covariance matrix used to weight the inversion. The mean LOS velocity is represented for the tracks 151 and 628 in the Figures 4.2 and 4.4 where motion away from the satellite is positive.

Table 2.1: Table summarizing the informations about the 4 tracks used in this study

Satellite and track	Number of interferograms used	Master epoch	Incidence angle (°)	Heading angle(°)	Mean looking vector (E/N/U)
Envisat 151	25	2005/06/17	23	-14.1221	(0.3706/0.0981/-0.9230)
Envisat 380	29	2005/10/16	23	-14.0621	(0.3727/0.0987/-0.9229)
ALOS 326	37	2007/12/18	39	-13.5889	(0.6087/0.1612/-0.7792)
ALOS 628	33	2008/03/01	39	-166.4245	(0.6087/0.1612/-0.7766)

2.3 Data analysis

2.3.1 External influences

As we can see in the Figure 2.2, the detrended time series at TAUP indicates that there are multiple tectonic and volcanic processes contributing to the observed observation. First, we identified two offsets caused by large earthquakes: the 8.1 Mw Macquarie Island earthquake occuring the December 23, 2004 (Watson et al., 2010) and the 7.8 Mw Kaikoura earthquake (Hamling et al., 2017) occuring the November 14, 2016 (number 1 and 7 respectively in Figure 2.2). Because these earthquakes occured outside of our observations period, we did not correct for them in our data. Also, the InSAR data (Figures 4.2 and 4.4) shows a widespread subsidence in the southern part of the central TVZ which has been interpreted as the consequence of magma cooling within the shallow crust (Hamling et al., 2015). These affected pixels will therefore be excluded from our models.

Slow slip events

Two deep slow slip events (SSE) have been identified and modeled at the central Hikurangi margin in 2006 and 2008 (Wallace and Eberhart-Phillips, 2013). Inversion results place the slip between 25 and 45 km depths on the subduction interface over a region about 50 km wide in

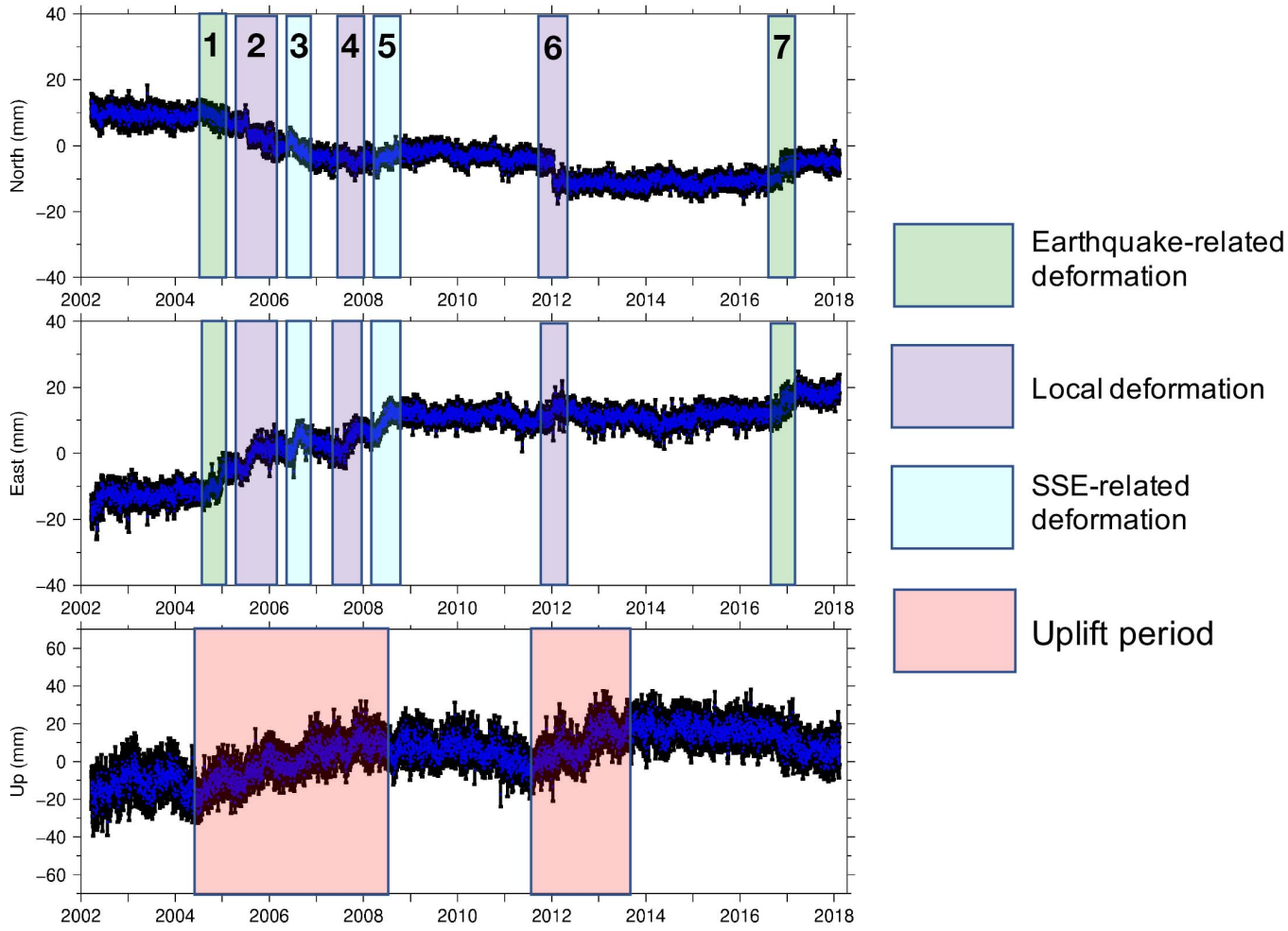

Figure 2.2: Detrended time serie of the TAUP CGPS station showing the different deformation episodes affecting the area.

the along-dip direction. Instead of interpolating the deformation induced by these events from our CGPS stations (number 3 and 5 in Figure 2.2), we decided to use the forward model of Wallace and Eberhart-Phillips (2013) in order to predict the displacements for the campaigns sites. However, for the 2006 event, the model doesn't provide a good fit to the CGPS data. As we just want to use it to correct the data, we decided to add a constant value to all of our sites that minimizes the misfit between model-predicted displacements and those estimated from the data. Predicted displacements by the scaled model are shown in red on the Figure 2.3 on the left.

In Figure (2.3) (right panel) we can see the different behaviour of the TAUP, TGOH and TGWH stations North and East of the lake, which may indicate that the 2008 deep SSE triggered local deformation in the area. This will be discussed in the next chapter.
The correction of tectonic events of regional impacts is relatively small. We have identified other deformation periods observed by the CGPS sites (Figure 4.8) whose origin is unknown.

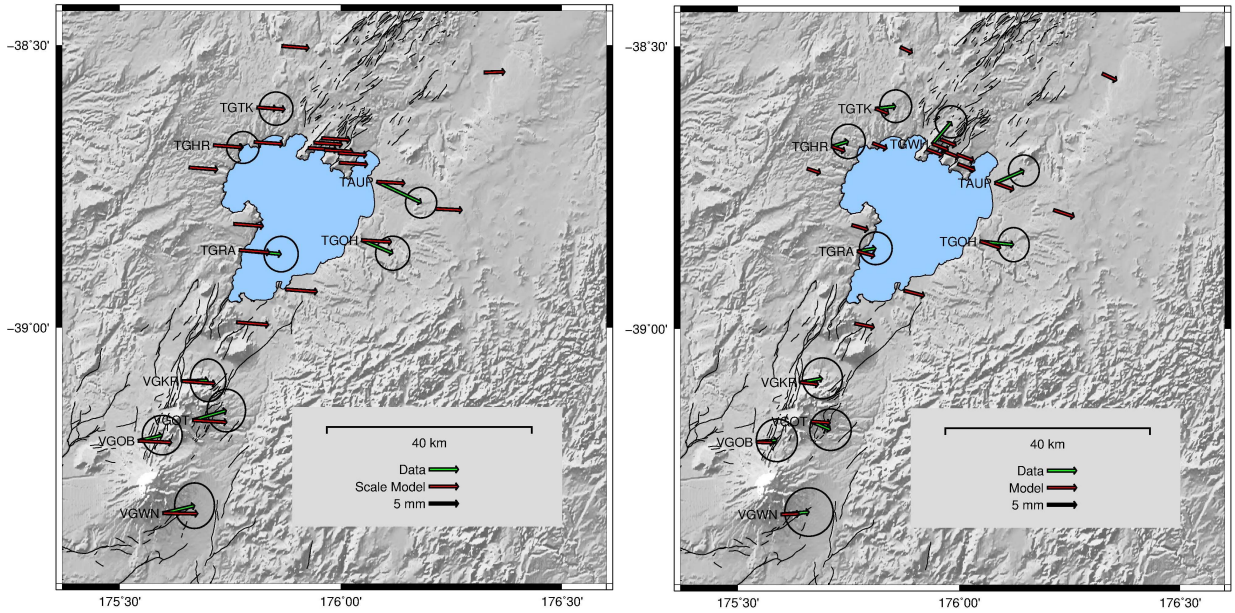

Figure 2.3: Observed (by the CGPS stations) and modeled displacements induced by the deep SSEs in 2006 and in 2008 on the left and on the right panel, respectively.

Geothermal stations

Another source of deformation affecting our data is generated by pumping water into the Wairaikei-Tauhara geothermal station (visible on the Figures 4.2 and 4.4 at about (176°05';-38°4')) which causes localized subsidence. Apart from station ARTA, the continuous GPS stations are too far away to be affected by this (ARTA shows a subsidence rate of more than 5 mm/yr as seen in Figure 2.1; this background deformation having been removed, we can consider that the ARTA station is corrected for this effect). However this significantly affects the InSAR data. We invert them to model the source of subsidence using the GBIS software ((Bagnardi and Hooper, 2018); the modeling strategy will be presented in the section 3.1). The best-fitting model consists of two horizontal rectangular tensiles sources (Okada, 1985) with a RMS of 1.124 mm/yr whose centers are represented by the black dots in the Figure 2.4. For Wairakei, it suggests a 1.2 ± 0.9 x 3.1 ± 1.2 km-source contracting at -2.5 ±1.8 10^5 m^3/yr at a depth of 1.8 ± 0.35 km, while for Tauhara it suggets a 1.4 ±0.8 x 1.2 ± 1.0 km-source contracting at -0.9 ± 0.5 10^5 m^3/yr at a depth of 2.4 ± 0.32 km.

2.3.2 Local deformation

Once external deformation sources have been estimated and removed from our data, local events can be revealed. First, we identified a 4-year uplift period between 2004 and 2008 in InSAR Envisat and CGPS data with up to 15 mm/yr (LOS velocity) (Figure 2.2). We can see that the uplift occurs in the Northeast corner area of the lake. Based on availability of GPS campaigns in the region, we investigated three additional time periods (Figures 3.2, 2.5). Offsets in the time series of continuous sites were estimated using the same dates as those when the measurements

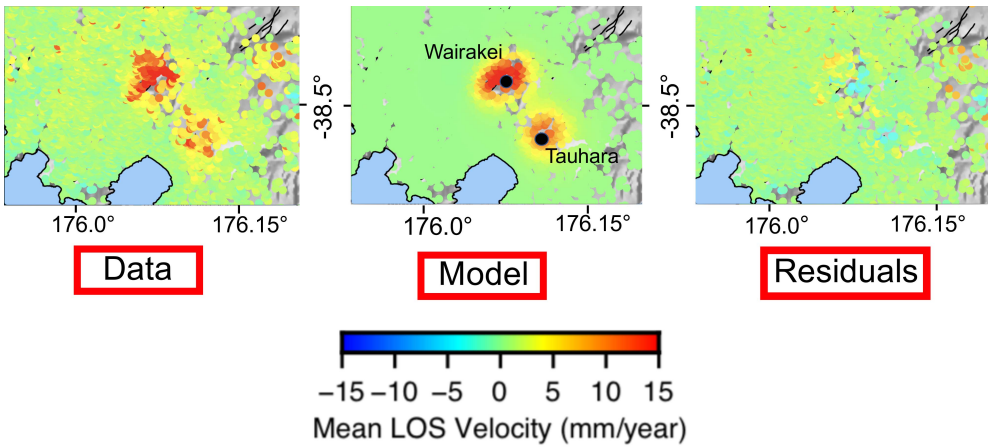

Figure 2.4: Observed, modeled and residual velocities for the subsidence at the Wairakei-Tauhara geothermal station. For this plot, data are those of the ALOS track 628. The two black points show the center of the best-fitting sill sources.

of the campaign sites were acquired. For the 2005-2007 period, there is local deformation north of the lake, located slightly to the west of the continuous uplift pattern from 2004 to 2008 (Figures 3.1, 3.2). Between 2007-2011, the horizontal deformation estimated by GPS shows up to 15 mm of displacement (Figure 2.5). This deformation is possibly the result of two distinct events. A local event was identified taking place over 40 days on September/August 2007 (Figure 2.2, part of the period 4) while local deformation is also observed following the deep SSE in 2008. The resulting deformation of these events is shown in Figure 3.3 and will be modeled separately. And finally the 2011-2015 period whose the horizontal deformation is shown in the Figure 2.5. For station 2406, which become continuous in 2012, we estimated the deformation between its last acquisition as a campaign site in 2011 and between 2012 (in green in the figure). We also add in red the GPS displacements linked to the 2012 event (Figure 2.2, period 6), which appears to be localized in the north-east of the lake.

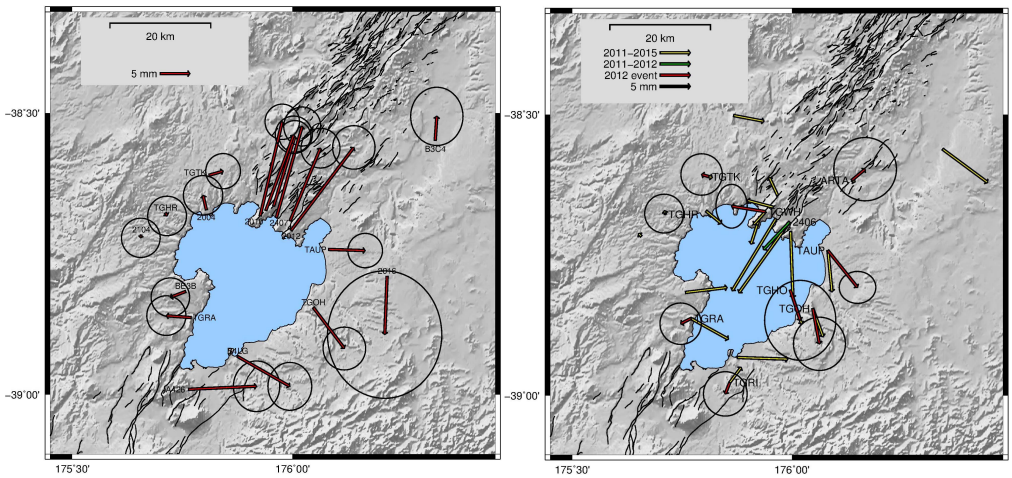

Figure 2.5: Left: GPS deformation for both continuous and campaigns sites between 2007 and 2011. Right: GPS deformation for the 2011-2015 period in yellow, for the 2011-2012 period in green and for the 2012 event in red.

3 | Modeling and interpretation

3.1 Modeling strategy

We performed the inversion of our geodetic data using GBIS (Geodetic Baysesian Inversion Software), a MATLAB-based software package (Bagnardi and Hooper, 2018). This bayesian approach allows the characterization of Posterior probability Density Functions (PDFs) of source model parameters. In GBIS, the inversion algorithm samples the posterior PDFs through a Markov Chain Monte Carlo (MCMC) method incorporating the Metropolis-Hastings algorithm. The posterior PDF sampled by the algorithm describes the probability associated with model parameters according to their ability to explain the data taking into account their uncertainties and considering any prior information. The GPS data errors are characterized by variances associated to each displacement component at each sites while the InSAR data errors are characterized by estimating a theoretical covariance function using an experimental semivariogram. In this study, different analytical forward models were tested, including: Mogi point source (Mogi, 1958), Okada horizontal dislocation (Okada, 1985), Mc-Tigue spherical source (McTigue, 1987) and the Yang prolate spheroid source (Yang et al., 1988). These different tests allow us to explore different possibilities of source geometry and to see how they explain the data. When GPS and InSAR data are used together for an inversion, we have chosen to increase the weight of GPS data by a factor of five to take into account the fact that there are many more InSAR points and to prevent them from completely dominating the inversion.

3.2 Results

For each period studied, the results of the inversions are listed in the Table 3.2.1 for each of the models tested. Letters stands for the name of the model used (M=Mogi, T=McTigue, S=Sill, Y=Yang).

3.2.1 2004-2008 period

For the 2004-2008 period, our best-fitting model is an ellipsoid source at 8.1±1.5 km depth increasing of 0.023±0.009 km^3 and dipping of 30±15°relative to East, represented in the Figure 3.1. The analysis of lake leveling data of Peltier et al. (2009) reveals two periods of lake tilting to the west in 1999-2001 and 2004-2007 interpreted as a consequence of inflating pressure sources at 11 ± 3 and 13 ± 4 km depth respectively, consistent with the location and amount of inflation from our inferred source for the period 2004-2008.

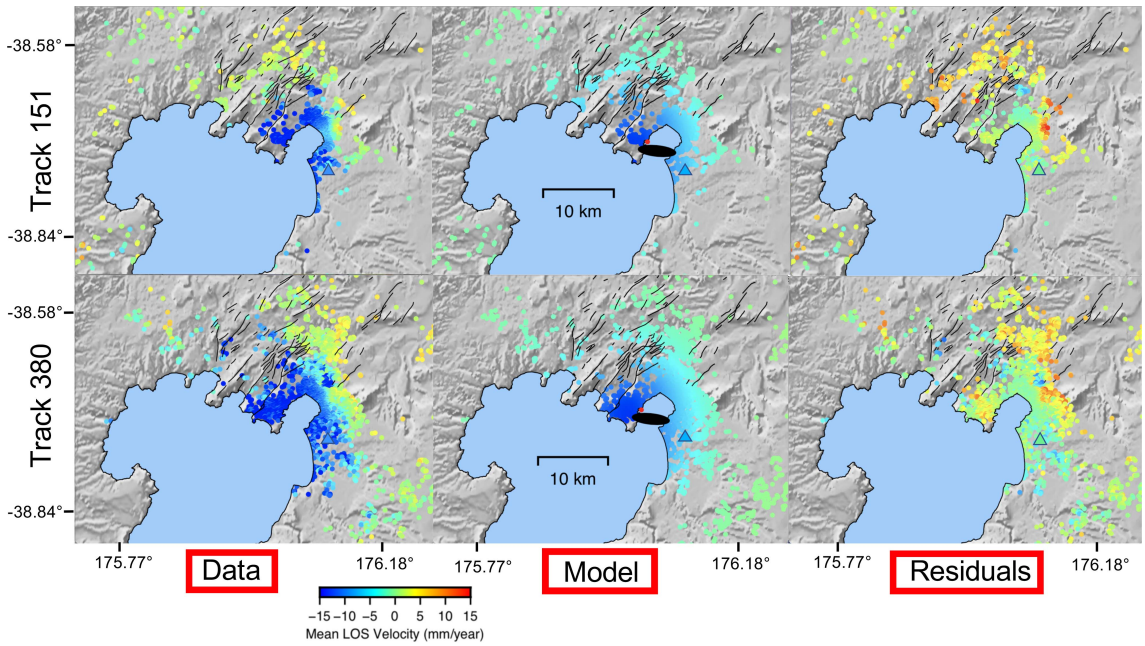

Figure 3.1: Observed, modeled and residual velocities during the 2004-2008 period for both Envisat tracks 151 and 380. The triangle indicates the LOS velocity estimation for the GPS TAUP station on the same time period. The best-fit location and geometry is represented by the black ellipse and the red dot indicates the location of both Mogi and McTigue sources.

3.2.2 2005-2007 period

Considering a simple source of inflation to explain the deformation observed over the 2005-2007 period, the inversion results show that this source would be located between about 4 and 7 km depth depending on the model. Again the best-fitting model is an ellipsoid source dipping of -3.23±2°relative to the East at 6.5±0.6 km (Figure 3.2) with a GPS RMS of 1.3 mm. Given the large errors associated with the vertical component of GPS survey data, the vertical component of the deformation observed is mainly constrained by InSAR data. For this, we used the estimated LOS velocity for the period 2004-2008, which we multiplied by two to obtain the equivalent of the deformation taking place in the two year period, between 2005 and 2007, assuming a linear velocity. The InSAR RMS is 2.8 mm for the ellipsoidal source which generates a spatial pattern of uplift quite similar to that observed for the whole period 2004-2008. In addition, as the deformation observed is located very close to the Kaiapo fault (Figure 3.2 on the right), we also try to model this period considering both an inflating ellipsoid source and motion along this fault (as the fault motion itself doesn't explain the data very well). The results suggest 5 cm of dip slip along a 10x5 km fault dipping 50° westward with a strike of 210° and an ellipsoid source at a depth of 5.6±0.7 km with a smaller volume change (about 0.0035 km^3) but almost no change in location. We obtain a GPS RMS of 1.15 mm and a InSAR RMS of 2.48 mm. Such behavior for this fault is also estimated for the periods 2001-2002 by Peltier et al. (2009) interpreted as the cause of changes in leveling measures. However a F-TEST shows that the improvement of the RMS by adding the parameters of the fault in the

Table 3.1: Table summarizing the inversion results. Letters stands for the name of the model used (M=Mogi, T=McTigue, S=Sill, Y=Yang). The ellipsoid dimension is of the form: major axis/minor axis. Except for the 2004-2008 period, RMS are those related to the horizontal component for GPS.

Time Period	Model used	Location (Lon/Lat)	Depth (km)	Dimension (km)	Volume change (km^3)	Strike angle(°)	RMS (mm)
	M	176.032/-38.709	8.9±1.6	-	0.019±0.007	-	2.45
2004/	T	176.032/-38.709	9.1±1.4	2.1±1.3	0.020±0.007	-	2.41
2008[1]	S	176.044/-38.722	10.1±1.5	7.9±2.1x3.6±2.2	0.017±0.009	40±160	2.8
	Y	176.048/-38.721	8.1±1.5	5.1±2.1/1.3±1.1	0.023±0.009	96±80	2.32
	M	176.014/-38.683	5.6±0.3	-	0.003±0.0004	-	2.06
2005/	T	176.014/-38.683	5.7±0.3	1.2±0.4	0.003±0.0005	-	2.02
2007	S	176.056/-38.648	4.3±0.5	14.1±0.6x9.4±1.3	0.005±0.0004	290±5	2.2
	Y	176.033/-38.677	6.5±0.6	6.9±1.6/1.3±0.7	0.005±0.0008	260±7	1.3
	M	175.927/-38.725	8.0±2.6	-	0.006±0.002	-	3.15
2007	T	175.926/-38.726	7.9±2.7	0.2±0.7	0.006±0.004	-	3.14
	S	175.941/-38.730	13.1±3.6	2.2±1.9x5.9±2.3	0.003±0.002	333±60	2.69
	Y	175.932/-38.747	9.6±3.7	0.7±2/0.1±0.4	0.005±0.006	143±38	2.65
	M	175.942/-38.789	0.57±2	-	0.002±0.0004	-	0.93
2008	T	175.942/-38.789	1.0±1.8	0.8±0.1	0.001±0.0004	-	0.93
	Y	175.941/-38.788	0.78±0.8	2±1.5/1.2±1.1	0.001±0.0005	250±33	0.92
	M	176.036/-38.7	6.6±2.3	-	0.004±0.0021	-	1.47
2012	T	176.035/-38.7	6.4±2.3	1.3±1.1	0.004±0.001	-	1.5
	S	176.001/-38.683	8.5±2.6	9.5±2.2x5.9±2.3	0.005±0.003	201±80	2.08
	Y	176.039/-38.714	9.5±2.1	10.1±4/2.1±2.5	0.0046±0.003	342±80	1.02

[1] For this period the RMS are estimated from the InSAR data in mm / yr. For the other periods, it is estimated in mm from the GPS horizontal component.

model does not significantly improve the fit to the data considering a false-rejection probability of 0.05.

3.2.3 2007-2011 period

The eastward motion observable in the Figure 2.2 (period 4) seems to be caused by two factors. There is a period of 56 days (June-August 2007) showing eastward movement regionally (Figure 4.8 on the right) which is then followed by some local deformation over 40 days (August-September 2007) represented in the Figure 3.3. Observed deformation (green vectors) is estimated from six CGPS operating during this period and the red vectors stand for the predicted deformation for the campaigns sites. The source seems to be located between 8 and 13 km depending on the geometry. The best-fitting model is the ellipsoid source at 9.6 ± 3.7

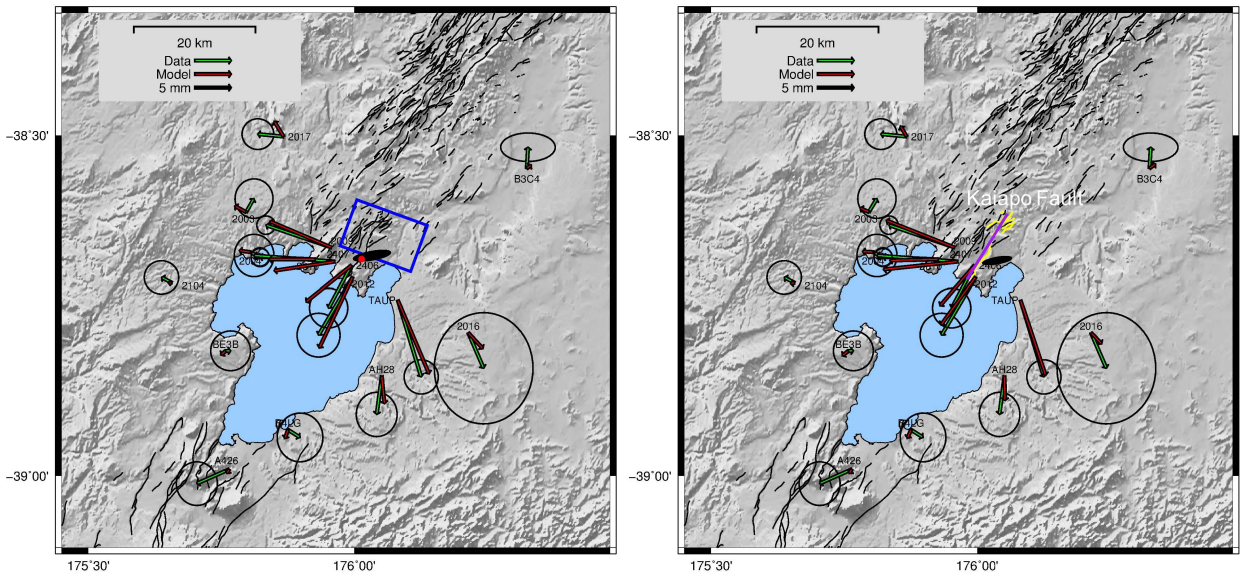

Figure 3.2: Left: Observed (green vectors) and modeled (red vectors) deformation during the 2005-2007 period for the best-fitting ellispoid source represented in black. We also represented the spheric source in red (corresponding to the Mogi source location as well) and the sill-like source in blue. Right: Observed and modeled deformation taking into account some motion on the Kaiapo fault in addition to the ellipsoid inflation source. The fault is colored in yellow and the purple line corresponds to the geometry used in the model. A F-TEST shows that the improvement of the RMS by adding the parameters of the fault in the model is not significant considering a false-rejection probability of 0.05.

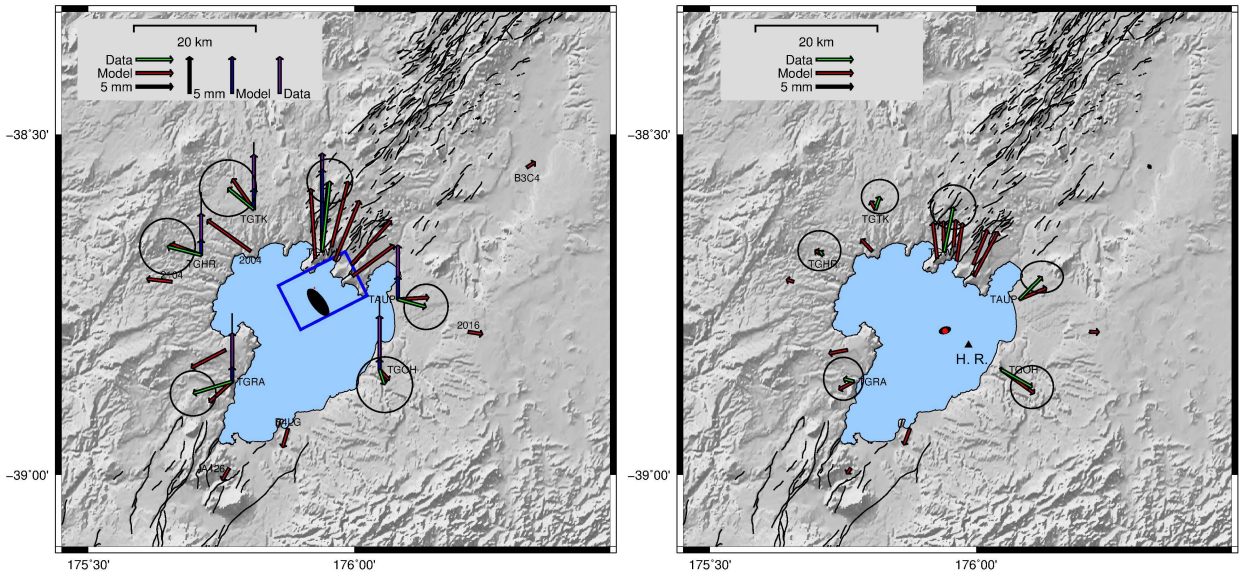

Figure 3.3: Left: Observed (green vectors) and modeled (red vectors) deformation during the 2007 event for the ellispoid source represented in black. We also represented the spherical source in red (corresponding to the Mogi source location as well) and the sill-like source in blue. Vertical bars represent the vertical uncertainty for CGPS. Right: Observed and modeled deformation during the 2008 event for the ellipsoid source represented in black. The spherical source is also represented in red and the black triangle stands for the Horomatangi Reef.

km increasing of 0.005±0.0008 km^3, dipping of -33±20° with a GPS RMS of 0.68 mm for the horizontal component and a InSAR RMS of 1.46 mm. However the spatial pattern from the predicted LOS displacements is no longer located in the northeast corner but just north of the lake. In the Figure 3.3, we can see the horizontal deformation observed (in green) by the CGPS between April-September 2008, beginning at the same time as the 2008 deep SSE which has been corrected. This close temporal relationship may suggest that the SSE triggered the local deformation event as proposed by Fournier et al. (2013). As it seems to reflect a regional phenomenon not related to this local deformation event, we excluded the CGPS vertical component when modeling the data. However, in addition to the horizontal GPS components, we used InSAR ALOS data covering the period 2007-2011. The results show a shallow source around 0.5-1 km of depth with a best-fitting ellipsoid source at 0.8 ±0.8 km increasing of 0.001±0.0005 km^3, dipping of -26 ±15° relative to the East. According to Jolly et al. (2008), between 40 and 50 mm of uplift was observed at Horomatangi Reef from March 2008 until February 2010 while our forward model gives 30 mm of uplift at this location (cf "H.R." in the Figure 3.3) over the 6 months period of observed deformation around the lake, which is quite consistent considering the uncertainties. This behavior is not an isolated case, indeed, an uplift is observed between 1996-1999 by lake leveling data which can be explained by a shallow over-pressurized source at 1±0.4 km in the area of the Horomatangi Reefs (Peltier et al., 2009). Comparing the predicted displacements for both 2007 and 2008 events, we note that their sum is quite similar to the estimated displacements during the whole period 2007-2011 for the north/north-east part of the lake (Figure 4.9). However, there is still unexplained deformation south of the lake for both stations A426 and B4LG.

3.2.4 2011-2015 period

The observed deformation corresponding to period six in the Figure 2.2 takes place in January 2012 in the north-east of the lake. There is an episode of rapid deformation with more than 3 mm offset in one day which then continues more slowly over approximately one month. The onset of the signal is not recorded at exactly the same time by different CGPS stations, it seems that the offset in the time serie of the TGOH station appears a day earlier than for the TAUP station. We can see that this event is linked to an uplift signal as well but we don't have available InSAR data to estimate the spatial extent of the signal. Therefore, we constrained our model only using the 9 CGPS stations operating at the time of the event, using both horizontal and vertical component. The best-fitting model is a 9.5 ±2.1 km deep ellipsoid source increasing of 0.0046±0.003 km^3, dipping of 35±20° East and located at a very similar place than the source estimated for the 2004-2008 inflation period (Figure 3.4). This fits the data with a RMS of 1.0 mm for the horizontal component and 2.8 mm for the vertical one. We also try to combine this source with some motion on the Kaiapo fault as for the 2005-2007 period and we obtain a RMS

of 1.0 mm. This episode of deformation also seems to be linked to shallow seismicity (Figure 3.4), occuring during the January month. A few days after the beginning of the deformation, three small events (1.8<Mw<2.2) took place just beneath our inferred source between 8 and 16 km (two of them are hidden behind the red spherical source, see Figure 4.13) and four others in the South part near TGRA station. At the end of the deformation signal, a seismic swarm took place in the middle of the northern part of the caldera, with 23 events recorded during about 10 hours with magnitutes ranging from 1.6 to 3 Mw and depth between 5 and 17 km. (https://www.geonet.org.nz/earthquake)
In Figure 3.4, we show the residuals between the predicted displacements caused by the 2012 event and those estimated between 2011 and 2015 for both campaigns and continuous sites. We can see that they are mainly dominated by an eastward movement which can be explained by ohters SSEs occuring in 2011 and 2013. However, both stations 2407 and 2406 have a different behaviour. As station 2406 becomes continuous following the 2012 event, it can be seen that this motion toward the South-West (shown in the Figure 2.5) is a quasi-continuous feature taking place until 2013. Such local behavior for this same station is also observed after the Kaikoura earthquake that triggered a shallow slow slip event at less than 15 km deep on the central and northern Hikurangi subduction margin (Wallace et al., 2017). We can see in the Figure 4.10 in red the deformation occuring one day after the Earthquake and in green the deformation during the next month due to the slow slip event. We can observe a quite different behavior for TGHO stations (which is more noisy) as well as for station 2406, which may suggest the presence of a very shallow local source. In May 2018 we conducted a short GPS field campaign in order to remeasure among others the 2407 station, located west of 2406. We estimated and compared the movements between 2015 and 2018 for the two stations. The same behavior is not observed at both stations and further analysis, including InSAR data would be necessary to understand the source of this signal.

4 | Discussion and conclusion

First, it is important to clarify the limitations of this study. The analytical models we use here assume simple geometries embedded in a homogeneous, isotropic and elastic half-space. Improvements can be made on this point for example by taking into account the structure of the caldera filled with weak rubble on a depth of 3 to 4 km. It has been shown that this can increase the surface deformation (Ellis et al., 2007). Also the presence of the lake prevents us from observing the surface deformation generated within the caldera and this adds ambiguity in the characterization of the geometry of the deformation source. When the geometry is poorly constrained, this can lead to less accurate estimates of the change in volume. Another improvements can me made adding the lake leveling data set to the inversion. In addition, we only use deformation observations here that we can interpret in terms of volume change in

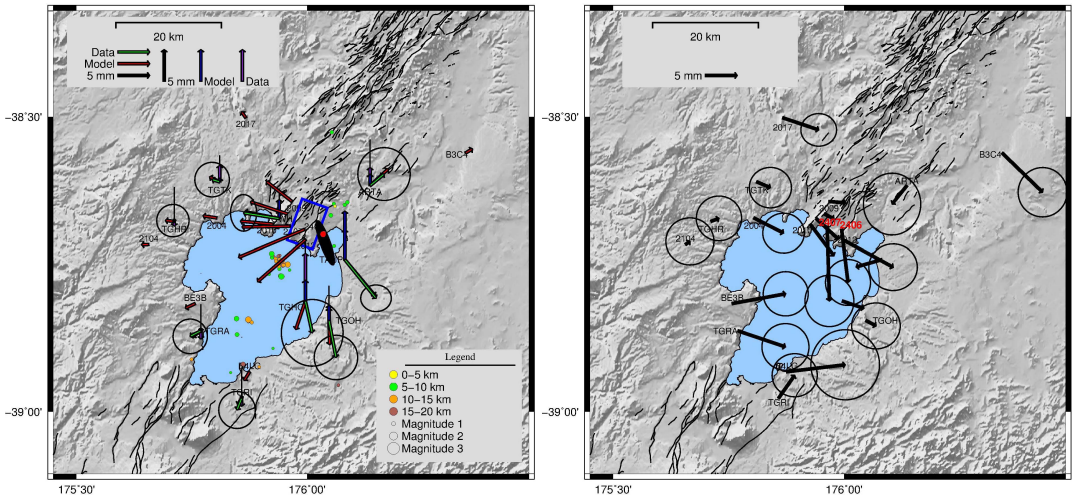

Figure 3.4: Left: Observed (green vectors) and modeled (red vectors) deformation during the 2012 event for the ellispoid source represented in black. We also represented the spheric source in red (corresponding to the Mogi source location as well) and the sill-like source in blue. Seismicity during the January month in 2012 is also represented. Right: Residuals between the predicted displacements caused by the 2012 event and the displacements estimated between 2011 and 2015.

depth but in the absence of gravity changes data it is impossible for us to know the density of the intruded fluid and thus to conclude less ambiguously on the cause of the deformation. It would be interesting to carry out new gravity measurements north of Lake Taupo to learn more about the current state of the shallow crust beneath the volcano.

However, this study allows us to reveal several periods of local deformation clearly different from the background deformation we estimated for the region. A first feature is the uplift occurring in the northeast corner of Lake Taupo, identified since the detection of changes in leveling measurements in 1999-2001, then characterized by InSAR data between 2004 and 2008 and again between 2011 and 2013 (but without InSAR data to characterize the extension of the uplift signal). These changes in the data are explained by an inflating source between 8 and 13 km deep depending on the period and the geometry of the source used. Also this is accompanied by horizontal deformation identified by the GPS data between 2005 and 2007 as well as in 2012. The results of the inversion for the period 2005-2007 seem to indicate a shallower source (between 4 and 7 km depth), slightly further west. Several hypotheses can be formulated to explain this. The signal may be due to a different process that is actually shallower (which may be related to changes in the deep part of the Wairakei-Tauhara geothermal system for example) whose location is poorly constrained. The subsidence signal identified between 2011 and 2015 is poorly explained by the model derived from the InSAR data and seems to indicate a deeper source than the 2 km obtained. Considering a magmatic source, this difference in location/depth may indicate lateral and vertical movements of magma between two sources, but taking into account the uncertainties in the data (intrinsic uncertainty and those related to the corrections made for the external deformation factors) and in the characterization of the

model parameters, we can also consider that this horizontal deformation is simply linked to the inflation of the same inferred source for the entire period 2004-2008. By observing in more detail the time serie of the TAUP station, one realizes that the deformation is not continuous during the 2 years but takes place mainly between July and September 2005 as well as more weakly between January and February 2006. However it is uncertain that these signals appear exactly at the same time for the campaign sites. In 2012 the deformation taking place in January is explained by a similar source than the one inferred for the period 2004-2008 with a seismic swarm of small 23 events at the end (Figure 4.13), the temporal relationship may suggest that it was the event in 2012 that triggered it. We also notice a seismic swarm of 25 1.6-2.9 Mw events between 5 and 12 km of depth north of the lake occuring in one day in September 2004, few months after the beginning of the uplift (cf Figure 4.12). However, other recent geophysical studies are not really conclusive about the presence of a deep magmatic body: from their 3-D seismic velocity and seismic attenuation study Bannister et al. (2015) observes low Vp (<5 km/s) along the north edge of Lake Taupo at 4 km of depth and variation between 5.3 and 6 km/s at 6 km; while MT data reveal a slightly greater resistivity in the uplift zone than in the surrounding area but not as much as that observed further north in the central TVZ, interpreted as a zone of interconnected melt (Heise et al., 2010). Yet, as already mentioned, the interpretation of the data is limited in this region by the presence of the lake and the 3-4 km volcanic infill. Two other sources at different locations are needed to explain the deformation observed between 2007 and 2011. The source supposed to be the cause of the 2007 event is located under the lake in the northern part of the caldera, at a similar depth than the source generating the 2004-2008 uplift and almost at the same location as the 2012 seismic swarm. A seismic swarm of 32 events also takes place quite close to the location of this source over 2 days in August 2008 ranging from 1.4 to 2.6 Mw and from 2 to 12 km of depth, the main part taking place at 5 km. (see Figure 4.13). While in 2008 the source explaining the deformation observed is very shallow (0.5-1 km) and localized fairly close to the geothermal system of Horomatangi Reef. A similar behavior is produced at the Campi Flegrei caldera, it is supposed that the deep part (∼2.5 km) of a geothermal reservoir inflates in response to mass and heat input from a magmatic source, which then triggers the migration of fluids into the shallower part (∼0.75 km) causing some uplift signal and shallow microseismicity as the fluids tend to reduce the resistance of the surrouding rocks (D'Auria et al., 2011*a*). In our case, the deep part inflation could be a response to the inflation of a magmatic body further north located at the position of the inferred source from the period 2004-2008 or to the inflation corresponding to the 2007 event a few months earlier. Also, a significant increase in the shallow seismicity during 2008-2010 is observed following the deformation event (cf Figure 4.11). This emphasizes the importance of studying hydrothermal systems, places of complex processes that can lead to unrest periods. Also, Fournier et al. (2013) proposes that the 2008 deep SSE triggered some readjustements at the caldera boundaries, with subsidence of the central part causing stress changes in the

underlying magmatic or hydrothermal system and finally resulting in the period of fluid-driven ground inflation observed and increased seismicity. We observe that the 2007 event is preceded by regional deformation pointing to the subduction trench and may reveal the occurrence of an SSE generating small but broad deformation signal.

To conclude, it is necessary to carry out the continuous monitoring of this volcano, by combining several geophysical data (geodetic, MT, seismic, heat flux, gas emanation for hydrothermal systems) in order to be able to satisfactorily know the current state of the volcano after the different periods of deformation documented in this report. It will also allows us to estimate at best the eventualities that periods of unrest will take place in the future.

References

Bagnardi, M. and Hooper, A. (2018), 'Inversion of surface deformation data for rapid estimates of source parameters and uncertainties: a Bayesian approach', *Geochemistry,Geophysics, Geosystems* .

Bannister, S., Bourguignon, S., Sherburn, S. and Bertrand, T. (2015), '3-D Seismic Velocity and Attenuation in the Central Taupo Volcanic Zone, New Zealand: Imaging the Roots of Geothermal Systems', *Proceedings World Geothermal Congress 2015* .

Beavan, J., Tregoning, P., Bevis, M., Kato, T. and Meertens, C. (2002), 'Motion and rigidity of the Pacific Plate and implications for plate boundary deformation', *Journal of Geophysical Research* **107**(B10), 2261.

Bibby, H., Caldwell, T., Davey, F. and Webb, T. (1995), 'Geophysical evidence on the structure of the Taupo Volcanic Zone and its hydrothermal circulation', *Journal of Volcanology and Geothermal Research* **68**(1), 29–58.

Bryan, C. J., Sherburn, S., Bibby, H. M., Bannister, S. C. and Hurs, A. W. (1999), 'Shallow seismicity of the central Taupo Volcanic Zone, New Zealand: its distributionand nature', *New Zealand Journal of Geology and Geophysics* **42**, 533–542.

Caldwell, T. G. and Bibby, H. M. (1992), 'Geothermal implications of resistivity mapping in Lake Taupo', *Proc. 14th N.Z. Geothermal Workshop 1992. University of Auckland* pp. 207–212.

Cole, J. (1990), 'Structural control and origin of volcanism in the Taupo volcanic zone', *Bulletin of Volcanology* **52**, 445–459.

Davy, B. W. and Caldwell, T. G. (1998), 'Gravity, magnetic and seismic surveys of the caldera complex, Lake Taupo, North Island, New Zealand', *Journal of Volcanology and Geothermal Research* **81**, 69–89.

De Ronde, C., Stoffers, P., Garbe-Schönberg, D., Christenson, B., Jones, B., Manconi, R., Browne, P., Hissmann, K., Botz, R., Davy, B., Schmitt, M. and Battershill, C. (2002), 'Discovery of active hydrothermal venting in Lake Taupo, New Zealand', *Journal of Volcanology and Geothermal Research* **115**, 257–275.

DeMets, C., Gordon, R. G. and Argus, D. F. (2010), 'Geologically current plate motions', *Geophysical Journal International* **181**, 1–80.

D'Auria, L., Giudicepietro, . F., Aquino, I., Borriello, G., Gaudio, C. D., Bascio, D. L., Martini, M., Ricciardi, G. P., Ricciolino, P. and Ricco, C. (2011*a*), 'Repeated fluid-transfer episodes as a mechanism for the recent dynamics of Campi Flegrei caldera (1989–2010)', *Journal of Geophysical Research* **116**(B04313).

D'Auria, L., Giudicepietro, F., Aquino, I., Borriello, G., Gaudio, C. D., Bascio, D. L., Martini, M., Ricciardi, G. P., Ricciolino, P. and Ricco, C. (2011*b*), 'Repeated fluid-transfer episodes as a mechanism for the recent dynamics of Campi Flegrei caldera (1989–2010)', *Journal of Geophysical Research* **116**(B04313).

Ellis, S. M., Wilson, C. J. N., Bannister, S., Bibby, H., Heise, W., Wallace, L. and Patterson, N. (2007), 'A future magma inflation event under the rhyolitic Taupo volcano, New Zealand: numerical models based on constraints from geochemical, geological, and geophysical data', *Journal of Volcanology and Geothermal Research* **168**, 1–27.

Fournier, N., Williams, C., Wallace, L., Sherburn, S., Jolly, A. D., Chardot, L., Ristau, J., Bourguignon, S., AW, A. W. H., Scott, B. J., Gibbs, M., Unglert, K. and Beavan, J. (2013), 'From subduction processes to volcanic unrest: unraveling domino effects at Lake Taupo caldera, New Zealand', *2013 AGU Fall meeting, 9–13 December* .

Hamling, I. J., Hreinsdottir, S. and Fournier, N. (2015), 'The ups and downs of the TVZ: Geodetic observations of deformation around the Taupo Volcanic Zone, New Zealand', *Journal of Geophysical Research: Solid Earth* **120**, 4667–4679.

Hamling, I. J., Hreinsdóttir, S., Clark, K., Elliott, J., Liang, C., Fielding, E., Litchfield, N., Villamor, P., Wallace, L., Wright, T., D'Anastasio, E., Bannister, S., Burbidge, D., Denys, P., Gentle, P., Howarth, J., Mueller, C., Palmer, N., Pearson, C., Power, W., Barnes, P., Barrell, D. J., Dissen, R. V., Langridge, R., Little, T., Nicol, A., Pettinga, J., Rowland, J. and Stirling, M. (2017), 'Complex multifault rupture during the 2016 Mw 7.8 Kaikōura earthquake, New Zealand', *Science* **356**(6334).

Heise, W., Caldwell, T. G., Bibby, H. M. and Bennie, S. L. (2010), 'Three-dimensionalelectrical resistivity image of magma beneath an active continental rift, Taupo Volcanic Zone, New Zealand', *Geophysical Research Letters* **37**.

Herring, T. (2003), 'MATLAB tools for viewing GPS velocities and time series', **7**, 194–199.

Hooper, A. (2008), 'A multi-temporal InSAR method incorporating both persistent scatterer and small baseline approaches', *Geophysical Research Letters* **35**.

Hooper, A., Segall, P. and Zebker, H. (2007), 'Persistent Scatterer InSAR for Crustal Deformation Analysis, with Application to Volcan Alcedo, Galapagos', *Journal of Geophysical Research* .

Jolly, G. E. R. J. B., Christenson, B. W., Ellis, S. M., Jolly, A. D., Miller, C. A., Peltier, A., Scott, B. J., Sherburn, S., Wallace, L. M. and McCaffrey, R. (2008), 'What constitutes unrest at Taupo caldera, New Zealand?', *2008 AGU Fall Meeting, 15–19 December* .

Kampes, B. M., Hanssen, R. F. and Persk, Z. (2008), 'A multi-temporal InSAR method incorporating both persistent scatterer and small baseline approaches', *Geophysical Research Letters* **35**.

McTigue, D. F. (1987), 'Elastic stress and deformation near a finite spherical magma body: resolution of the point source paradox', *Journal of Geophysical Research: Solid Earth* **92**(B12), 12931–12940.

Mogi, K. (1958), 'Relations between the eruptions of various volcanoes and the deformation of the ground surface around them', *Bull. Earthquake Res. Inst.* **36**, 99–134.

Okada, Y. (1985), 'Surface deformation due to shear and tensile faults in a half-space', *Bulletin of the seismological society of America* **75**(4), 1135–1154.

Peltier, A., Hurst, A. W., Scott, B. J. and Cayol, V. (2009), 'Structures involved in the vertical deformation at Lake Taupo (New Zealand) between 1979 and 2007: new insights from numerical modelling', *Journal of Volcanology and Geothermal Research* **181**, 173–184.

Potter, S. H., Scott, B. J., Jolly, G. E., Johnston, D. M. and Neall, V. E. (2015), 'A catalogue of caldera unrest at Taupo Volcanic Centre, New Zealand, using the Volcanic Unrest Index (VUI)', *Bulletin of Volcanology* .

Rosen, P. A., Hensley, S., Peltzer, G. and Simons, M. (2004), 'Updated repeat orbit interferometry package released', *Eos Transactions AGU* **85**, 47.

Rowland, J. V., Wilson, C. J. and Gravley, D. M. (2010), 'Spatial and temporal variations in magma-assisted rifting, Taupo Volcanic Zone, New Zealand', *Journal of Volcanology and Geothermal Research* **190**(1), 89–108.

Stratford, W. and Stern, T. (2004), 'Strong seismic reflections and melts in the mantle of a continental back-arc basin', *Geophysical Research Letters* **31**.

Stratford, W. and Stern, T. (2006), 'Crust and upper mantle structure of a continental backarc: Central North Island, New Zealand', *Geophysical Journal International* **166**(1), 469–484.

Sutton, A. N., Blake, S., Wilson, C. J. N. and Charlier, B. L. A. (2000), 'Late Quaternary eruption of a hyperactive rhyolite magmatic system: Taupo volcaninc centre, New Zealand', *Journal of the Geological Society* **157**(2000), 537–552.

Villamor, P. and Berryman, K. (2001), 'A late Quaternary extension rate in the Taupo Volcanic Zone, New Zealand, derived from fault slip data', *New Zealand Journal of Geology and Geophysics* **44**, 243–269.

Wallace, L. M., Beavan, J., McCaffrey, R. and Darby, D. (2004), 'Subduction zone coupling and tectonic block rotations in the North Island, New Zealand', *Journal of Geophysical Research* **109**.

Wallace, L. M. and Eberhart-Phillips, D. (2013), 'Newly observed, deep slow slip events at the central Hikurangi margin, New Zealand: Implications for downdip variability of slow slip and tremor, and relationship to seismic structure', *Geophysical Research Letters* **40**, 5393–5398.

Wallace, L. M., Kaneko, Y., Hreinsdottir, S., Hamling, I., Peng, Z., Bartlow, N., D'Anastasio, E. and Fry, B. (2017), 'Large-scale dynamic triggering of shallow slow slip enhanced by overlying sedimentary wedge', *Nature Geosciences* .

Watson, C., Burgette, R., Tregoning, P., White, N., Hunter, J., Coleman, R., Handsworth, R. and Brolsma, H. (2010), 'Twentieth century constraints on sea level change and earthquake deformation at Macquarie Island', *Geophysical Journal International* **182**, 781–796.

Whiteford, P. (1996), 'Heat flow in the sediments of Lake Taupo, New Zealand', *Tectonophysics* **257**, 81–92.

Wilson, C., Houghton, B. F., McWilliams, M. O., Lanphere, M. A., Weaver, S. D. and Briggs, R. M. (1995), 'Volcanic and structural evolution of Taupo volcanic zone, New Zealand: a review', *Journal of Volcanology and Geothermal Research* **68**, 1–28.

Wilson, C. J. N. (2001), 'The 26.5 ka Oruanui eruption, New Zealand: an introduction and overview', *Journal of Volcanology and Geothermal Research* **112**, 133–174.

Yang, X. M., Davis, P. M. and Dieterich, J. H. (1988), 'Deformation from inflation of a dipping finite prolate spheroid in an elastic half-space as a model for volcanic stressing', *Journal of Geophysical Research: Solid Earth* **93**(B5), 4249–4257.

Acknowledgements

I would like to thank Sigrun Hreinsdottir and Ian Hamling for their support in my work by advising me and being available to answer my questions. I also thank Neville Palmer and Rory Hart for taking me with them during the GPS campaign. And thanks to Laura Wallace for providing her model predicting the displacements due to the SSEs. Finally, thanks to the Département des Géosciences de l'Ecole Normale Supérieure for the financial help.

Appendix

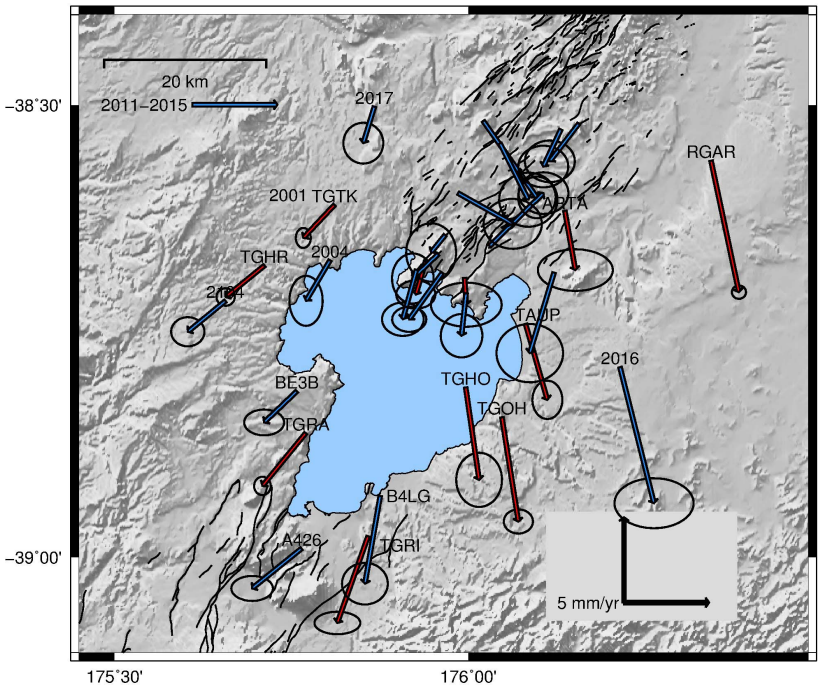

Figure 4.1: Background deformation estimated from the continuous GPS site (in red) and from the campaign sites for the 2011-2015 period in blue.

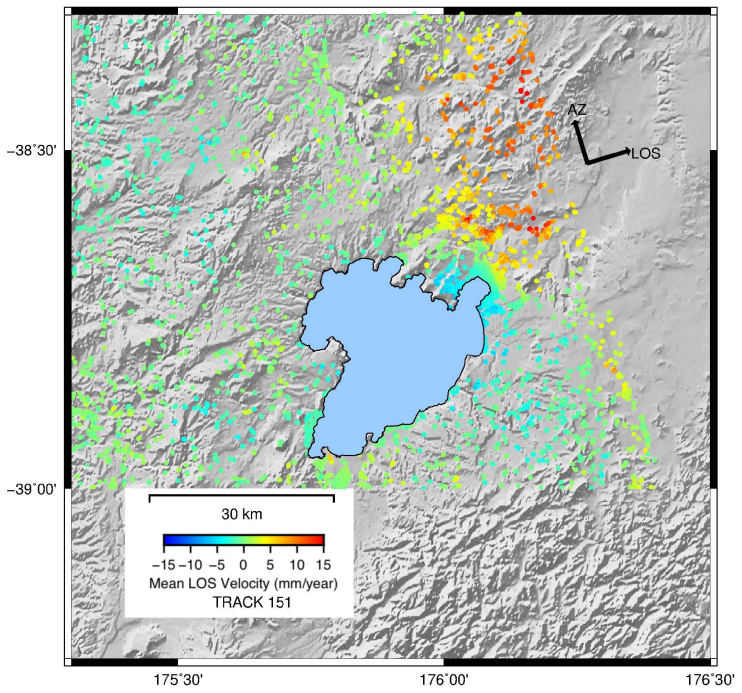

Figure 4.2: Mean LOS velocities derived from Envisat track 151 (on the left) during the 2003-2011 period.

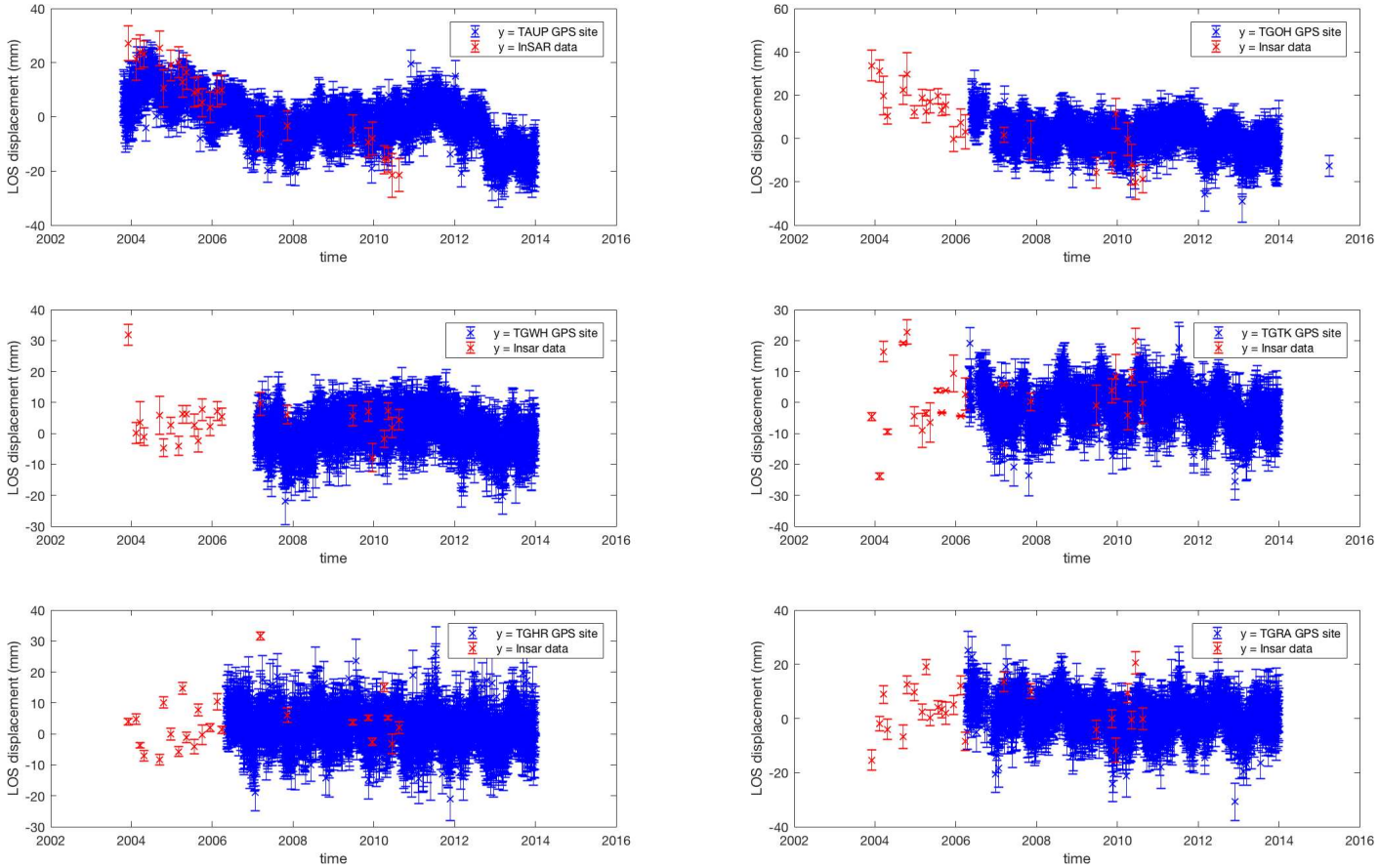

Figure 4.3: Comparison between InSAR data for the Envisat track 151 and six continuous GPS sites around the lake converted into the Line of sight of the satellite.

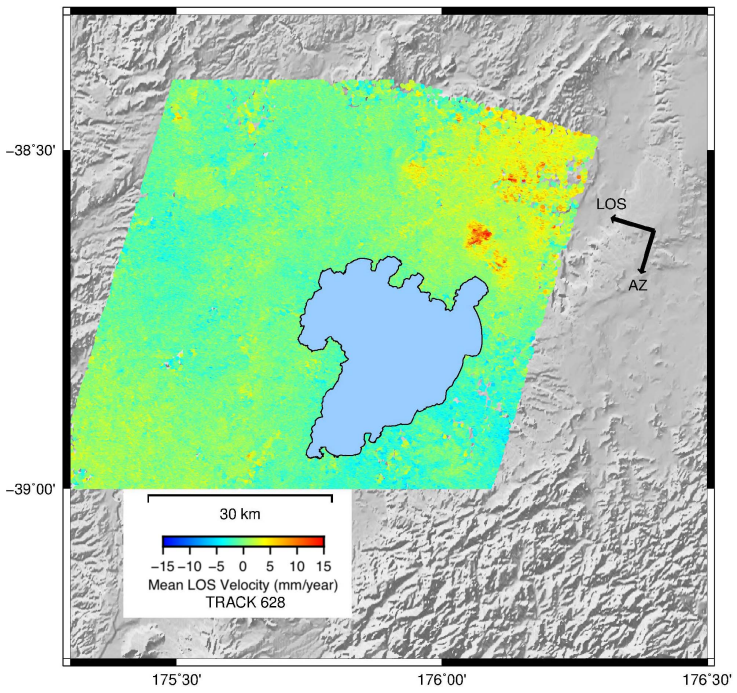

Figure 4.4: Mean LOS velocities derived from ALOS track 628 (on the right) during the 2007-2011 period.

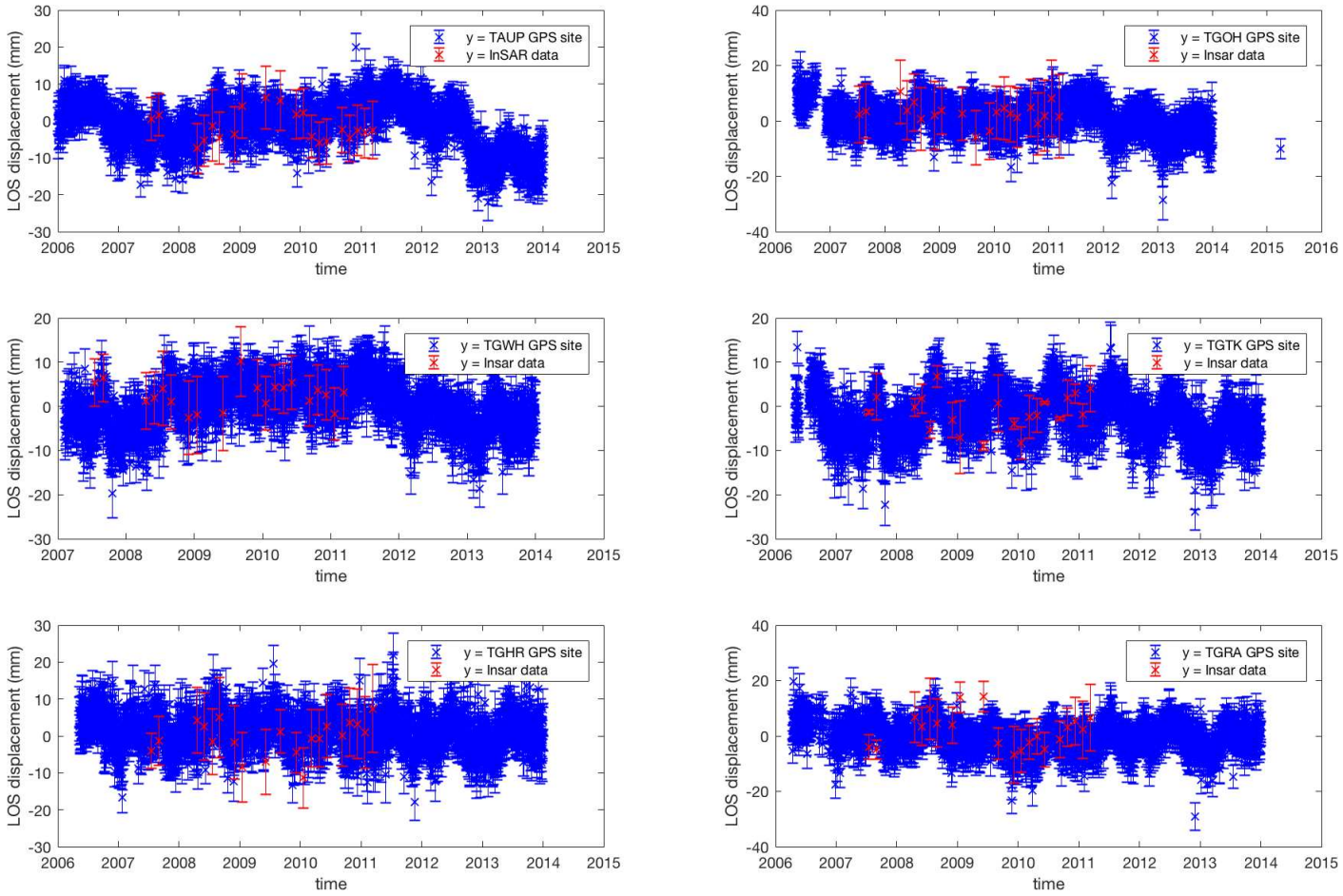

Figure 4.5: Comparison between InSAR data for the ALOS track 628 and six continuous GPS sites around the lake converted into the Line of sight of the satellite.

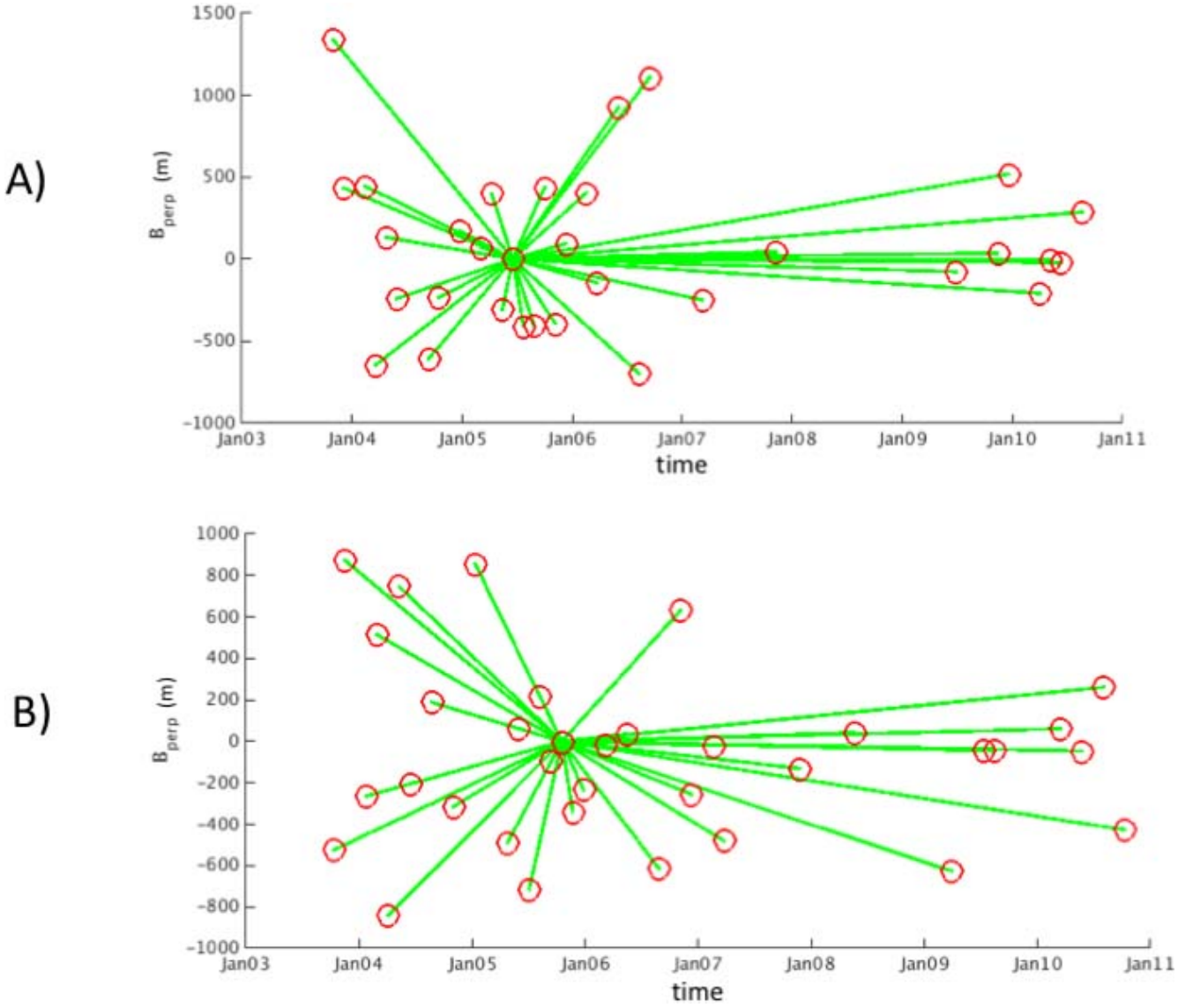

Figure 4.6: Perpendicular baselines versus time for Envisat data: A) track 151 and B) track 380

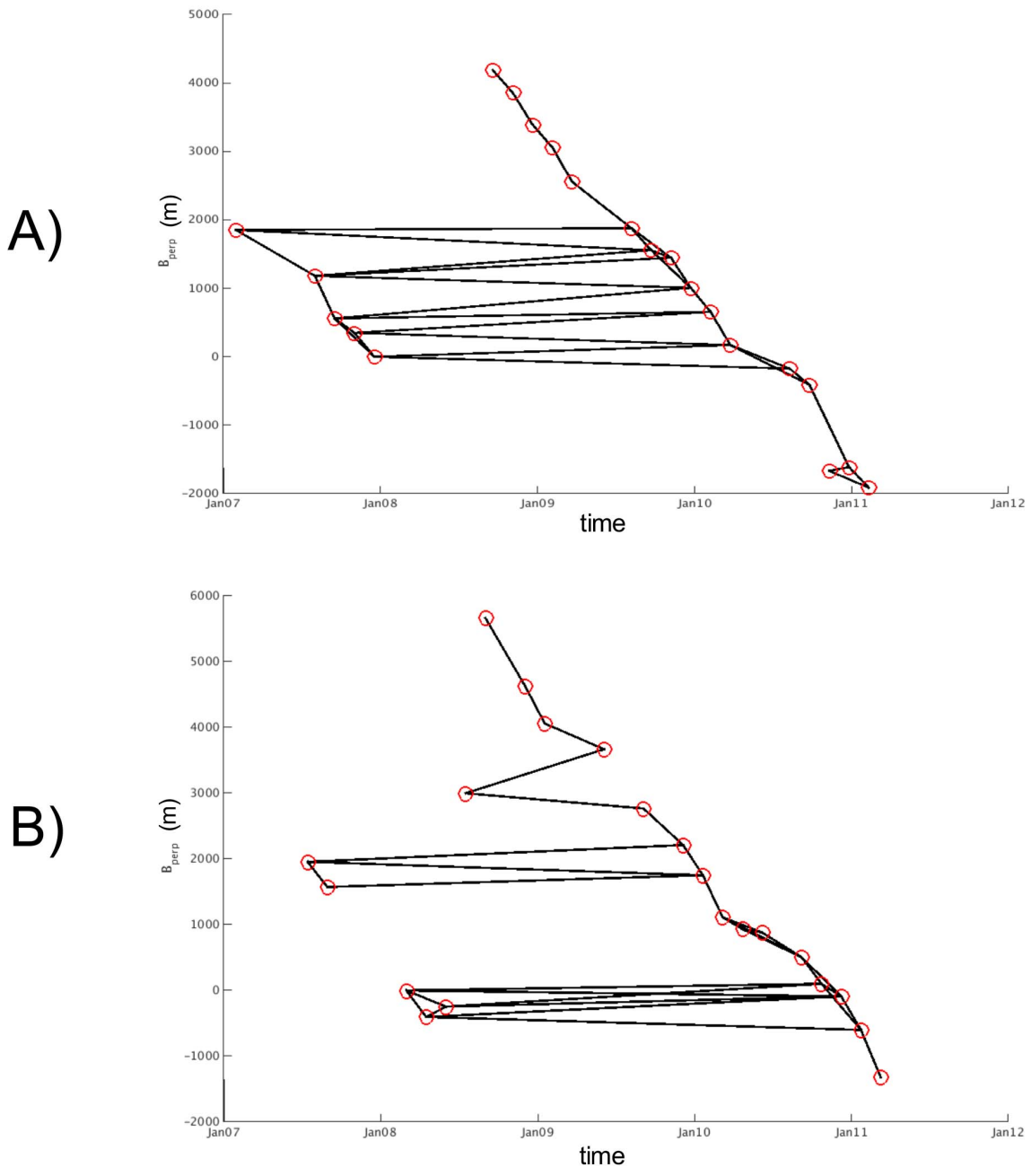

Figure 4.7: Perpendicular baselines versus time for ALOS data: A) track 326 and B) track 628

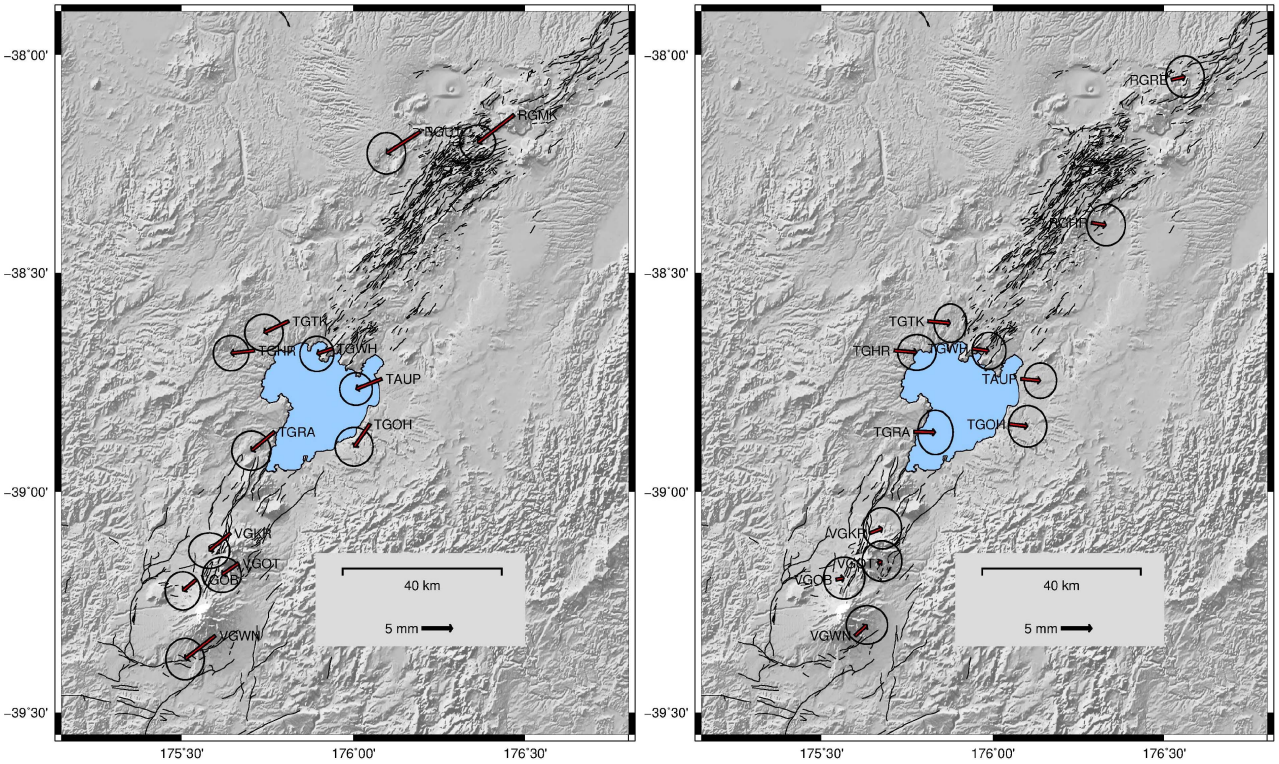

Figure 4.8: Left: Regional deformation observed over 280 days between Setptember 2006 and June 2007 of unknown origin. It corresponds to the period between the numerous 3 and 4 in the Figure 2.2. Right: Regional deformation observed over 56 days between June and August 2007, pointing towards the subduction trench.

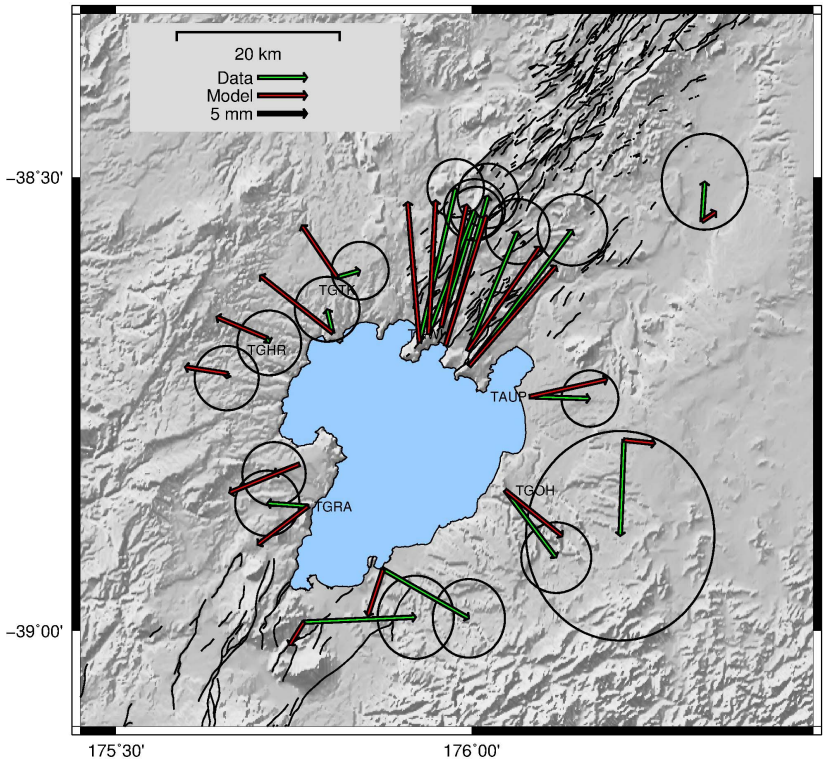

Figure 4.9: Observed (green vectors) and modeled (red vectors) displacements between 2007 and 2011. The predicted displacements represent the sum of the 2007 and 2008 event.

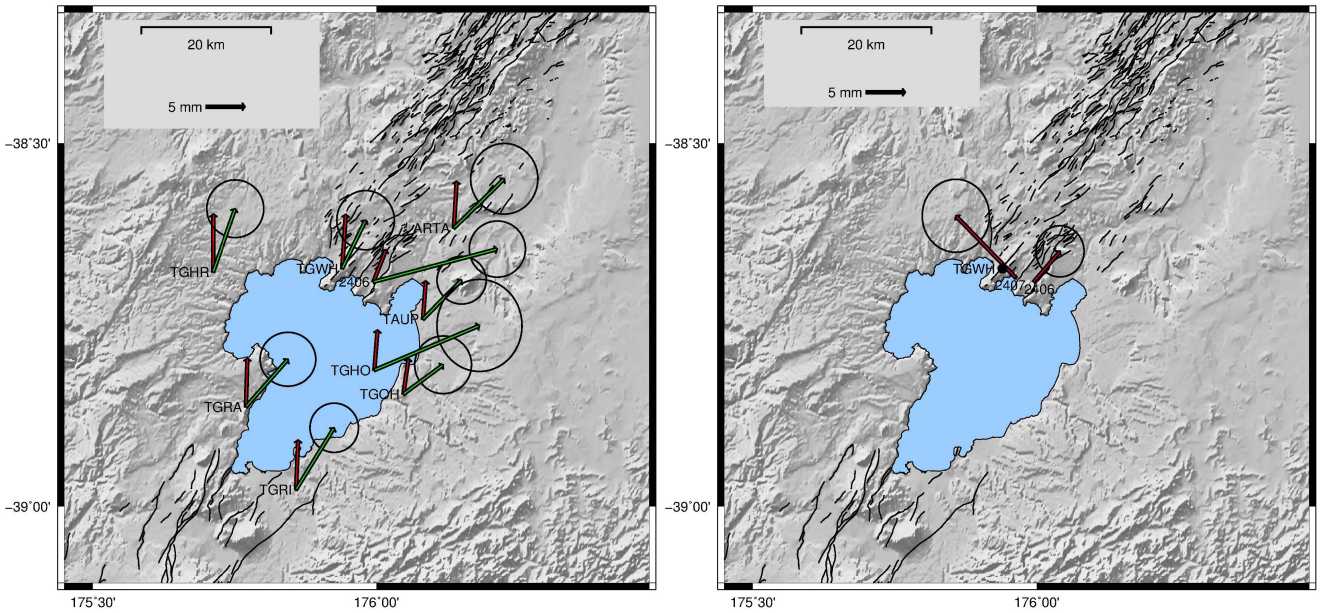

Figure 4.10: Left: Displacements estimated for CGPS, in red corresponding to the Kaikoura earthquake deformation and in green corresponding to the deformation until one month after, including eastward motion generated by a shallow SSE triggered by the Kaikoura earthquake. Right: Displacements relative to the TGWH station (represented by the black dot) between 2015 and 2018 for the 2406 CGPS site and the 2407 campaign site.

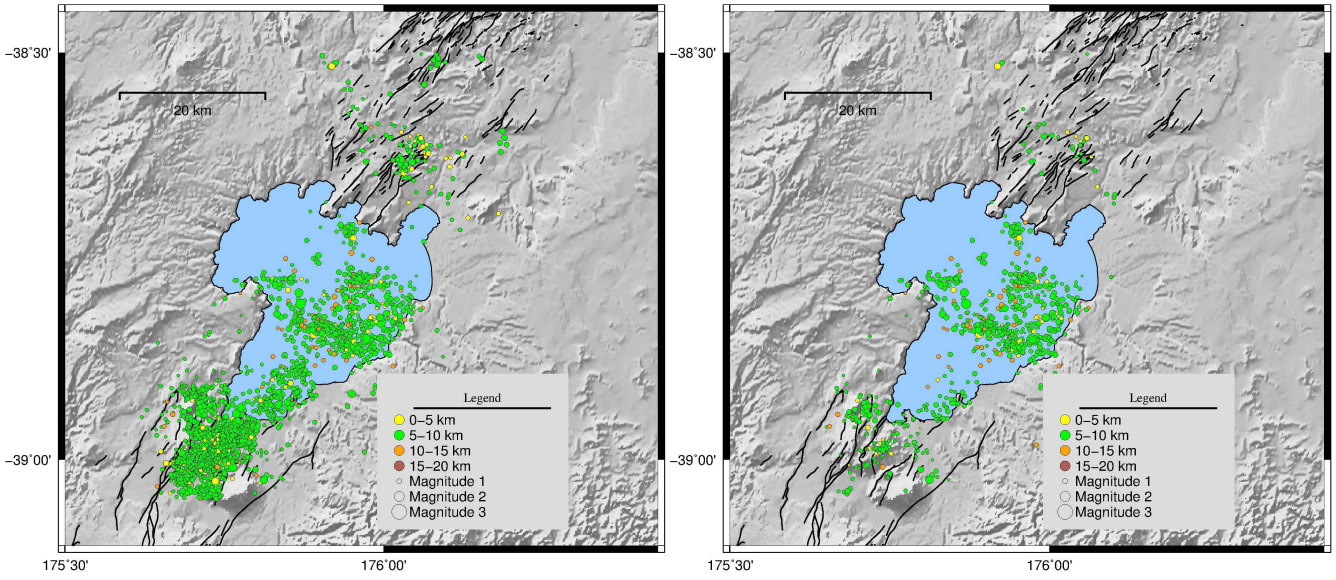

Figure 4.11: Left: Shallow seismicity (<20km) between April 2008 and February 2010. Right: Shallow seismicity during the 6 months where we observe the local deformation generated by the shallow source.

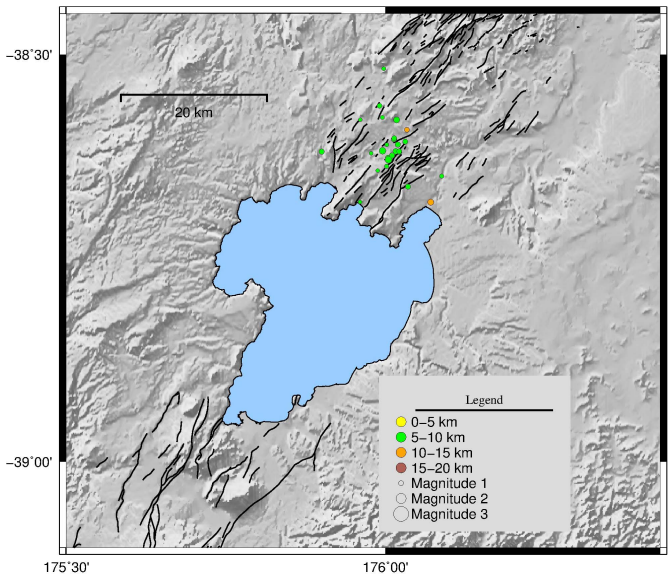

Figure 4.12: Seismic swarm of 25 events occuring the 14 September 2004.

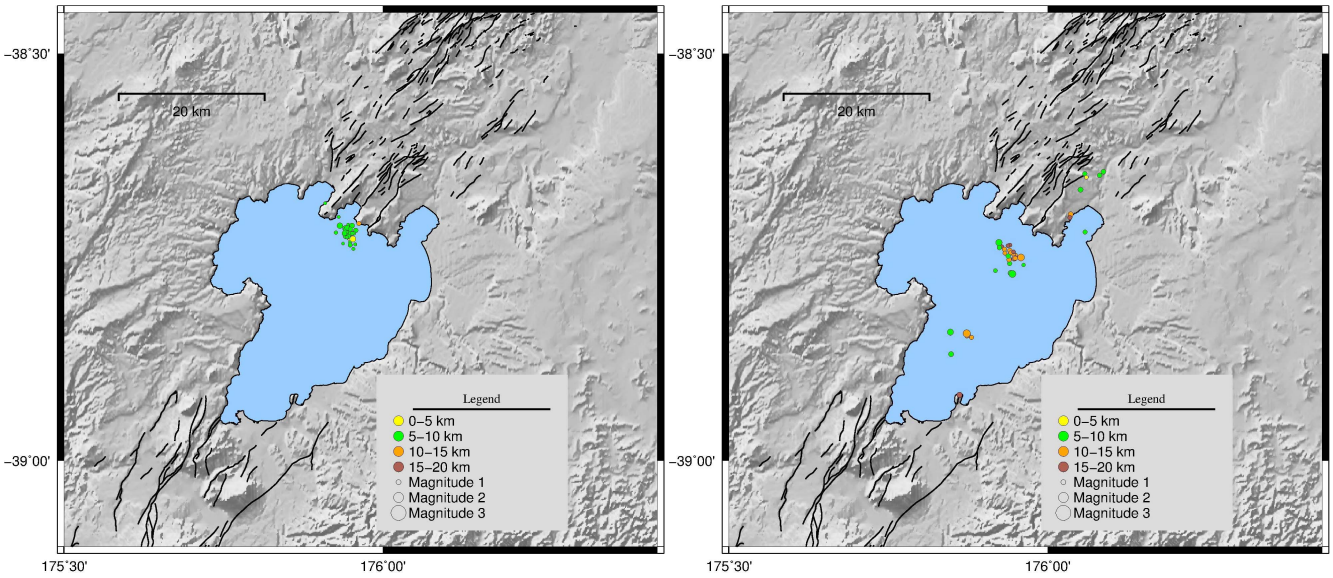

Figure 4.13: Left: Seismic swarm of 32 events occuring the 07/08 August 2008. Right: Seismic swarm of 23 events occuring the 22 January 2012.